https://doi.org/10.5194/egusphere-2026-4987
Preprint. Discussion started: 1 September 2026

A unified explicit formula for temperature-, pressure-, and composition-driven reaction-front propagation

Liudmila Khakimova[1], Stefan M. Schmalholz[1], and Yury Y. Podladchikov[1]
[1]Institute of Earth Sciences, University of Lausanne, 1015 Lausanne, Switzerland
Correspondence: Liudmila Khakimova (liudmila.khakimova@unil.ch)

Abstract. Metamorphic reactions, phase transitions, and fluid–rock interactions play key roles in many geodynamic processes. Such reactions can be driven by changes in temperature, pressure, or chemical composition, and hence by different thermodynamic variables, yet commonly propagate through rocks as moving reaction fronts. However, no unified theory predicts their propagation. Here, we show that reaction front propagation can be described within a single conservative moving-boundary framework. The theory couples diffusive transport with local equilibrium thermodynamics through the Rankine–Hugoniot condition and yields explicit analytical expressions for reaction-front position and velocity. Unlike classical Stefan-like solutions, which generally involve error functions and numerical solutions of a transcendental equation, our formulation directly relates front propagation to transport properties and equilibrium thermodynamics. The theory predicts the characteristic square-root-of-time, $\sqrt{t}$, scaling observed for temperature-, pressure-, and composition-driven fronts and shows that the diffusivity governing front propagation generally differs from the physical transport diffusivity. Instead, an effective front diffusivity combines diffusive transport with the thermodynamic transformation across the front. This combination is quantified by a dimensionless L number linking equilibrium thermodynamics to front dynamics. Consequently, slow front propagation does not necessarily imply slow transport but may reflect large changes in thermal energy or mass associated with the reaction. Furthermore, sharp reaction fronts can propagate under diffusion-dominated conditions because finite thermodynamic jumps are explicitly represented at the moving interface, unlike conventional advection–diffusion–reaction models, in which sharp fronts typically require advection-dominated transport. The framework provides a unified basis for predicting and interpreting reaction-front propagation in experiments and geological systems.

1 Introduction

Metamorphic reactions, fluid–rock interactions, and phase transitions, such as serpentinite dehydration, eclogitization, and magma crystallization, play fundamental roles in a wide range of geodynamic processes (Austrheim, 1987; Schmidt and Poli, 1998; Turcotte and Schubert, 2014; Philpotts and Ague, 2022). Fluid–rock interactions are also central to many applied problems, including geological carbon dioxide storage through mineral carbonation (Matter and Kelemen, 2009), hydrothermal ore formation (Ding et al., 2018), and leaching of geomaterials (Mainguy and Coussy, 2000). For brevity, we use the term *reaction* to collectively refer to metamorphic reactions, fluid–rock interactions, and phase transitions. These reactions are driven by changes in temperature, pressure, and/or chemical composition (Philpotts and Ague, 2022) (Fig. 1a). As a reaction propagates

https://doi.org/10.5194/egusphere-2026-4987
Preprint. Discussion started: 1 September 2026

through a rock or another material, it is commonly associated with the migration of a reaction front separating reacted from unreacted material (Stefan, 1891; Austrheim, 1987; Padrón-Navarta et al., 2011; Fusseis et al., 2012; Beinlich et al., 2020; Penniston-Dorland, 2025; Amiri et al., 2026) (Fig. 1b and c). Despite their different thermodynamic driving mechanisms, these processes therefore share the common feature of a propagating reaction front. Quantifying the velocity of such fronts and identifying the parameters controlling their propagation within a unified theoretical description remain major challenges.

A classical example of a temperature-driven moving phase boundary is the Stefan problem, which describes processes such as the freezing of water and crystallization of magma (Stefan, 1891; Gupta, 2017; Turcotte and Schubert, 2014). Temperature evolution is governed by thermal diffusion, whereas the position of the moving phase boundary constitutes an additional unknown. Its velocity follows from conservation of thermal energy, including latent heat, across the moving interface. The classical analytical solution typically involves the error function and the numerical solution of a transcendental equation (Gupta, 2017; Turcotte and Schubert, 2014). Stefan-like approaches have also been applied to composition-driven reaction fronts, including diffusion-controlled precipitation, dissolution, and leaching (Lichtner et al., 1986; Mainguy and Coussy, 2000; Coussy, 2004). In these systems, conservation of mass of the transported chemical component across the moving interface determines the front velocity. Accounting for this mass conservation is particularly important because reactions can produce abrupt changes in solid density, fluid content, porosity, and chemical composition across the front (Hacker, 2003; Malvoisin et al., 2015).

Pressure-driven reactions in fluid–rock systems can be formulated within the same moving-boundary concept (Khakimova et al., 2026). For a pressure-driven reaction, fluid pressure acts as the thermodynamic variable controlling equilibrium, whereas gradients in fluid pressure drive porous fluid flow (Malvoisin et al., 2015; Schmalholz et al., 2020; Bras et al., 2023; Mazzucchelli et al., 2024; Schmalholz et al., 2024; Mazzucchelli et al., 2026). Conservation of total mass across the reaction front then provides the additional condition required to determine its motion (Khakimova et al., 2026). Such pressure-driven fronts can occur during hydration and devolatilization reactions, including eclogitization of granulite and dehydration of serpentinite or gypsum (Fusseis et al., 2012; Bras et al., 2023; Schmalholz et al., 2024; Porkoláb et al., 2025). Thus, temperature-, pressure-, and composition-driven reaction fronts can all be formulated as moving-boundary problems coupling diffusive transport with thermodynamic transformations. The brucite–periclase reaction with pure water as fluid, for example, depends on temperature, pressure, and composition, here represented by water content (Fig. 2), and can therefore be driven by variations in any of these variables. However, no unified theory currently predicts front propagation for all three driving mechanisms and quantifies the parameters controlling the front velocity.

An important indication of a common underlying dynamics is the characteristic square-root-of-time scaling of reaction-front position, $x_F \propto \sqrt{t}$, known from classical Stefan problems (Stefan, 1891; Turcotte and Schubert, 2014). This scaling is observed experimentally and in natural systems for temperature-, pressure-, and composition-driven processes, including phase transitions, dehydration reactions, leaching, and carbonation (Fig. 3). The common $\sqrt{t}$ scaling therefore provides a natural basis for describing these apparently different reaction-front processes within a unified mathematical framework. The coefficient relating front position, x_F, to $\sqrt{t}$ has units of diffusivity (m^2/s) and can be interpreted as an effective front diffusivity. Importantly, this effective front diffusivity need not equal the physical diffusivity governing thermal, hydraulic, or chemical diffusive transport. Front propagation depends not only on transport but also on the finite thermodynamic transformation required as one

https://doi.org/10.5194/egusphere-2026-4987
Preprint. Discussion started: 1 September 2026

equilibrium state is replaced by another across the moving reaction front. An explicit relation between these two diffusivities is therefore essential for interpreting reaction-front propagation.

The distinction between transport diffusivity and effective front diffusivity is particularly relevant for experimental and natural observations. Constraints on the spatial and temporal evolution of reaction fronts in natural rocks are often limited, for example to estimates of the time required to form a reaction zone of a given thickness (John et al., 2012; Taetz et al., 2018; Beinlich et al., 2020). Inferring a transport diffusivity or permeability directly from such front propagation may therefore be misleading if the thermodynamic transformation across the reaction is neglected. An explicit analytical relation between front propagation, transport properties, and equilibrium thermodynamic results would allow such observations to be interpreted quantitatively and would clarify why slowly propagating reaction fronts do not necessarily imply slow physical transport.

Here, we show that temperature-, pressure-, and composition-driven reaction fronts share the same conservative moving-boundary structure. We couple diffusive transport to results of local equilibrium thermodynamics through conservation across the moving interface and derive explicit analytical expressions for reaction-front position, velocity, and effective diffusivity. The solutions avoid the error function and numerical solution of a transcendental equation characteristic of classical Stefan-like solutions, providing a direct relation between front propagation, transport properties, and equilibrium thermodynamics. The derivation further identifies the dimensionless numbers governing the different reaction mechanisms; for temperature-driven phase transitions, it naturally recovers the inverse of the classical Stefan number. The analytical expressions can be directly combined with equilibrium thermodynamic calculations based on Gibbs energy minimization and demonstrate that sharp reaction fronts can develop under purely diffusive transport without requiring advection. To test the approximations underlying the new explicit analytical solution, we compare the analytical solution with one-dimensional (1D) numerical simulations of pressure-driven hydration of periclase to brucite and composition-driven hydration of forsterite to antigorite.

https://doi.org/10.5194/egusphere-2026-4987
Preprint. Discussion started: 1 September 2026

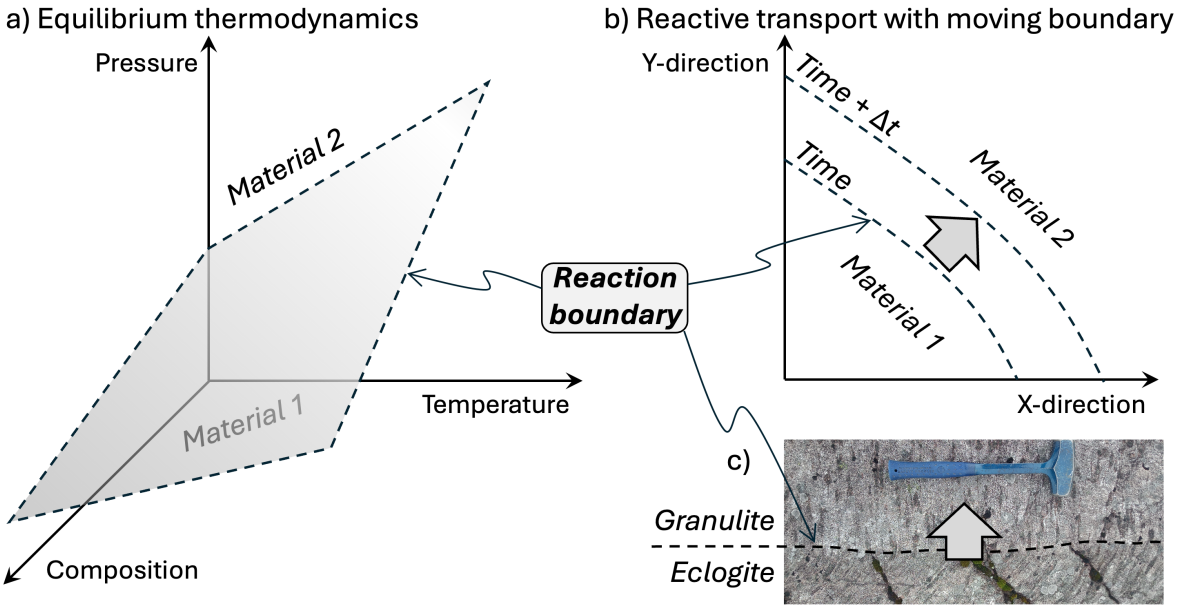

Figure 1. Sketch of a reaction boundary separating material 1 (below the boundary plane) and material 2 in temperature–pressure–composition space (a) and its propagation in two-dimensional physical space, where material 2 transforms into material 1 across the moving boundary (b). (c) Natural sharp reaction boundary between granulite and eclogite formed by hydration-driven transformation of granulite to eclogite. Photo courtesy of E. Bras.

https://doi.org/10.5194/egusphere-2026-4987
Preprint. Discussion started: 1 September 2026

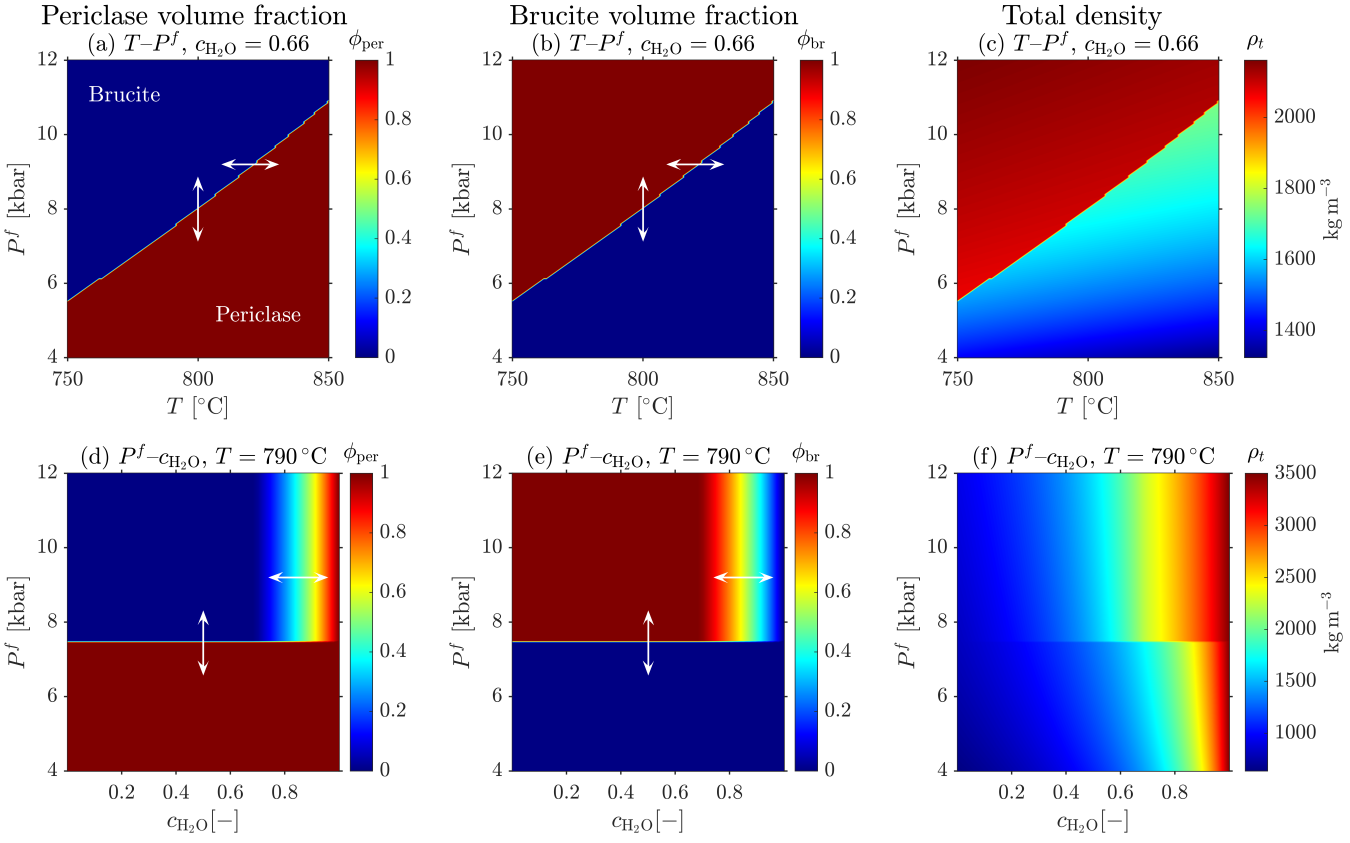

Figure 2. Results of thermodynamic calculations for the brucite–periclase–water system using ThermoLab (Vrijmoed and Podladchikov, 2022). Color maps show the equilibrium fractions of periclase (ϕ_{per}) and brucite (ϕ_{br}), and the total system density (ρ_t). Panels (a)–(c) show variations in temperature–fluid pressure (T–P^f) space at fixed bulk water content (c_{H_2O}), and panels (d)–(f) in c_{H_2O}–P^f space at $T = 790\,°C$. The transition between periclase- and brucite-dominated assemblages defines the (de)hydration reaction boundary, with the associated density change shown in panels (c) and (f). White arrows illustrate reaction trajectories driven by changes in pressure (vertical), temperature [horizontal in (a)–(c)], or composition [horizontal in (d)–(f)].

https://doi.org/10.5194/egusphere-2026-4987
Preprint. Discussion started: 1 September 2026

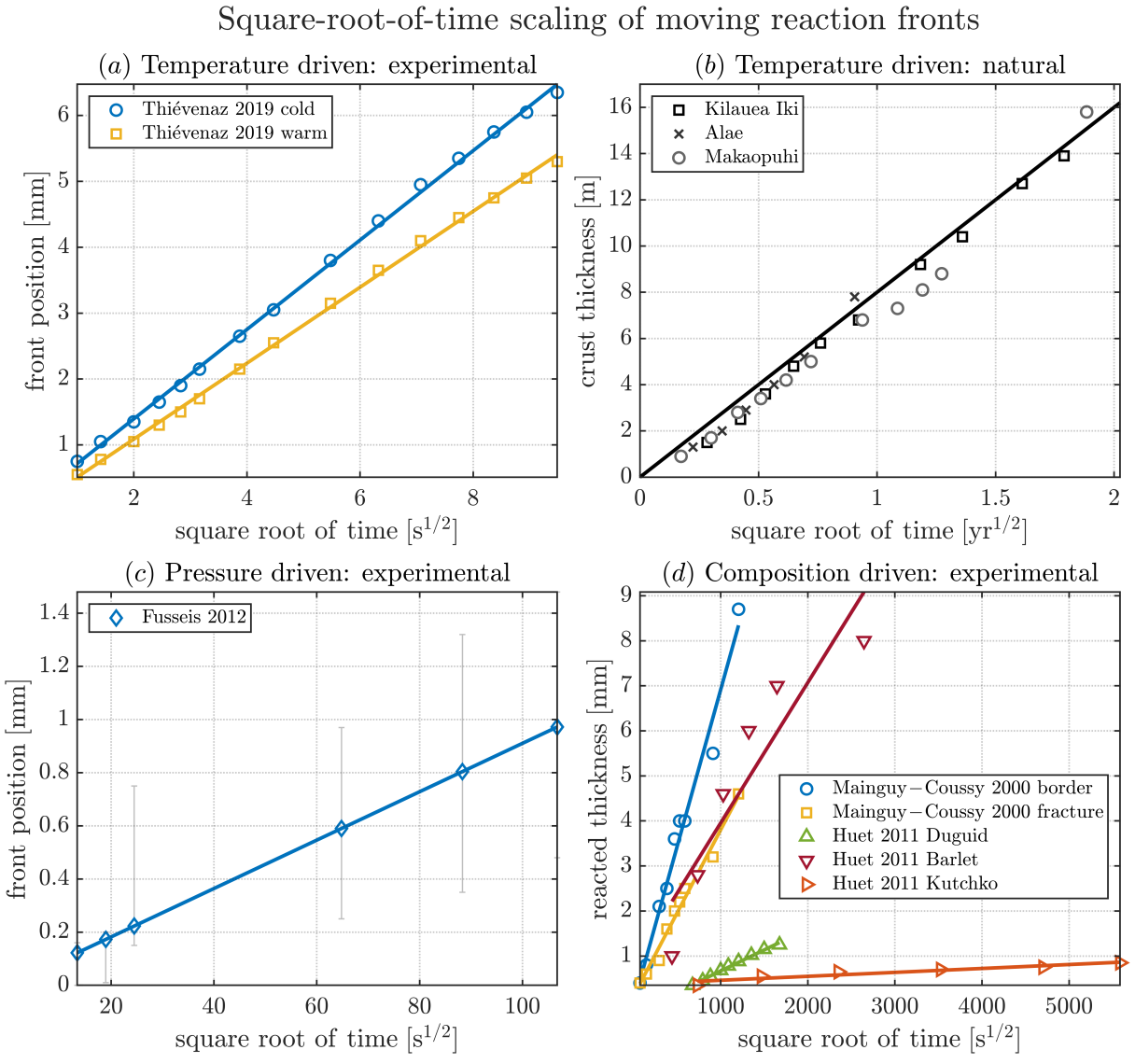

Figure 3. Square-root-of-time scaling of observed reaction-front propagation for different driving mechanisms: (a) laboratory temperature-driven solidification, (b) natural lava-lake solidification generating a solidifying crust, (c) experimental pressure-driven dehydration/de-volatilization of gypsum, and (d) experimental composition-driven dissolution, leaching, and carbonation. Reaction-front position or reacted-layer thickness (vertical axes) is plotted against the square root of time. Symbols show digitized or reported data, and solid lines show linear fits. Data are from: (a) solidification-front measurements from Fig. 3b of Thiévenaz et al. (2019) ("Thiévenaz 2019 cold" and "Thiévenaz 2019 warm"); (b) lava-lake solidification from Fig. 4-33 of Turcotte and Schubert (2014) ("Kilauea Iki", "Alae", and "Makaopuhi"); (c) gypsum dehydration from Fig. 5b of Fusseis et al. (2012) ("Fusseis 2012"); and (d) calcium leaching/degradation from Fig. 10 of Mainguy and Coussy (2000) ("Mainguy–Coussy 2000 border" and "Mainguy–Coussy 2000 fracture") and cement carbonation from Fig. 3 of Huet et al. (2011) ("Huet 2011 Duguid", "Huet 2011 Barlet", and "Huet 2011 Kutchko").

https://doi.org/10.5194/egusphere-2026-4987
Preprint. Discussion started: 1 September 2026

2 Derivation of explicit analytical solution

2.1 Moving-boundary approach

This section introduces an analytical framework for reaction fronts as moving-boundary problems. A reaction front is treated as an interface separating two local equilibrium states, whose position must be determined together with the transported field. This formulation provides a common mathematical description of temperature-, pressure-, and composition-driven reaction fronts despite their different driving mechanisms.

To obtain explicit analytical solutions, we employ a quasi-steady approximation and determine the front velocity by conservation of the relevant extensive quantity across the moving interface. Detailed derivations are provided in the Appendix; here, we focus on the resulting propagation laws and their application to temperature-, pressure-, and composition-driven reaction fronts.

2.2 Advection–diffusion–reaction within a fixed-boundary domain

The evolution of spatially distributed properties in fluid–rock systems is commonly described using advection–diffusion–reaction–type transport equations (McKenzie, 1984; Lichtner, 1996; Ferry and Gerdes, 1998; Ague, 2014; Penniston-Dorland, 2025). Away from a sharp reaction interface, the evolution of a scalar field $u(x,t)$ can be written in one spatial dimension as

$$\frac{\partial u}{\partial t} + v_a \frac{\partial u}{\partial x} - D\frac{\partial^2 u}{\partial x^2} = 0, \tag{1}$$

where v_a is the advection velocity and D is the transport diffusivity for the field u (see Table 1 for explanation of symbols). The variable u may represent different physical quantities depending on the process considered, for example, temperature, fluid pressure, chemical potential, or fluid concentration.

Under a quasi-steady approximation, the transient equation reduces locally to

$$v_a \frac{du}{dx} - D\frac{d^2 u}{dx^2} = 0. \tag{2}$$

This equation can provide the instantaneous spatial profile of the transported field near a prescribed reaction-front position (Fig. 4a and Appendix A), but it cannot predict the velocity of the front.

We consider a reaction front located at $x = x_F(t)$ and assume that it propagates in the positive x-direction. With this convention, the material already transformed by the reaction is located behind the front, $x < x_F(t)$, whereas the unreacted material is located ahead of the front, $x > x_F(t)$. For any field or material property q, we denote the one-sided values at the moving interface by

$$q_- \equiv q(x_F^-, t), \qquad q_+ \equiv q(x_F^+, t). \tag{3}$$

Here, x_F^- and x_F^+ denote spatial positions immediately behind and ahead of the reaction front, respectively (Fig. 4a). Accordingly, q_- is the value of q on the reacted side of the front, and q_+ is the value of q on the unreacted side.

https://doi.org/10.5194/egusphere-2026-4987
Preprint. Discussion started: 1 September 2026

The difference in q across the reaction front, hereafter referred to as the jump, is denoted by square brackets as

$$[q] \equiv q_- - q_+. \tag{4}$$

This convention is used throughout the paper.

For notational simplicity, the subscripts $-$ and $+$ are used only when distinguishing between the two sides of the front is necessary. Unsubscripted parameters denote values behind the advancing front or representative constant values for a given application. Under this convention, local thermodynamic equilibrium at the reaction front is expressed by the partition condition

$$u_- = k_{\mathrm{eq}}\, u_+, \tag{5}$$

where u is the transported field and k_{eq} is the equilibrium partition coefficient. If $k_{\mathrm{eq}} = 1$, u is continuous across the front. If $k_{\mathrm{eq}} \neq 1$, u_- and u_+ are different, but their ratio is fixed by local thermodynamic equilibrium (Fig. 4a).

For true thermodynamic potentials, such as temperature, fluid pressure, or chemical potential, local equilibrium usually gives $k_{\mathrm{eq}} = 1$. In this case, the potential is continuous across the reaction front. A fluid concentration may also be treated in this way when it is used as a monotonic proxy for chemical potential, for example under a fixed activity model or an ideal dilute approximation (Nauman and He, 2001). By contrast, solid concentrations, total component concentrations, phase fractions, and other phase-related variables are generally not thermodynamic potentials themselves. Their one-sided equilibrium values may differ across the reaction boundary, which corresponds to $k_{\mathrm{eq}} \neq 1$ and produces a finite jump in u. Thus, the same equilibrium partitioning condition describes both continuous and discontinuous front behavior, depending on the physical meaning of u.

We assume that advection and diffusion occurs only behind the front while the region ahead of the front is in an ambient equilibrium state with constant parameters. The solution of Eq. (2), subject to the front equilibrium constraint (5), admits the closed-form exponential profile of a variable u derived in Appendix A (Eq. A5). Its shape is controlled by the Peclet number, $Pe = v_a L_c / D$, where L_c is the characteristic length scale of the region behind the front. The corresponding asymptotic profiles are shown in Fig. 4a. In the diffusion-dominated limit, $Pe \ll 1$, the exponential solution reduces to an approximately linear profile behind the front. In the advection-dominated limit, $Pe \gg 1$, the variation of u is localized near the reaction front and forms an exponential boundary layer of thickness $\delta = D/v_a$. The jump of u at the front is controlled by the equilibrium relation (5), whereas the profile shape behind the front is controlled by the transport balance in Eq. (2).

The distinction between the transport profile and the jump condition is central to the moving-boundary problem. The quasi-steady advection–diffusion solution describes the transported field for a prescribed front position but does not determine the front position, $x_F(t)$, which follows from an additional conservation condition at the moving interface. The same moving-boundary framework can be extended to the full advection–diffusion problem; the corresponding quasi-steady profile is derived in Appendix A and given in Eq. (A5). However, determining the associated front dynamics requires resolving the advective boundary-layer structure and is left for future work. We therefore focus on the diffusion-dominated limit, $Pe \ll 1$, which retains the essential coupling between diffusive transport, local equilibrium, and conservation at the front while allowing an explicit analytical solution for reaction-front propagation. This minimal formulation makes the common mathematical structure of temperature-, pressure-, and composition-driven reaction fronts transparent.

https://doi.org/10.5194/egusphere-2026-4987
Preprint. Discussion started: 1 September 2026

Table 1. Notation used in the generalized moving-boundary formulation. Subscripts $-$ and $+$ denote one-sided values across the reaction front and are retained where required by the Rankine–Hugoniot condition. Unsubscripted transport parameters refer to the reacted domain or to representative constants for a given application. In the unit column, "p.d." denotes process dependent.

Symbol	Meaning	Unit
$x_F(t)$	Position of the moving reaction front	m
v_F	Reaction-front velocity, $\frac{dx_F}{dt}$	$\mathrm{m\,s^{-1}}$
$-$	Subscript denoting a one-sided value behind the reaction front, on the reacted side	–
$+$	Subscript denoting a one-sided value ahead of the reaction front, on the unreacted side	–
$[\cdot]$	Jump operator across the reaction front; for any quantity q, $[q] = q_- - q_+$	p.d.
u	Transported field driving reaction-front propagation	p.d.
u_-, u_+	One-sided values of the transported field behind and ahead of the front	p.d.
u_{BC}	Imposed boundary value of the transported field behind the front	p.d.
Δu	Driving-field contrast across the reacted domain, $u_{\mathrm{BC}} - u_-$	p.d.
$A(u)$	Conserved quantity per unit bulk volume	p.d.
A_-, A_+	One-sided values of $A(u)$ behind and ahead of the reaction front	p.d.
$[A]$	Conserved-quantity jump from the state ahead of the front to the state behind it, $A_- - A_+$	p.d.
A'_u	Derivative of $A(u)$ with respect to u, evaluated in the reacted domain, $\frac{dA}{du}$	p.d.
K	Transport coefficient, evaluated in the reacted domain	p.d.
D	True diffusivity, evaluated in the reacted domain, $\frac{K}{A'_u}$	$\mathrm{m^2\,s^{-1}}$
D_{eff}	Effective diffusivity, $\frac{K\Delta u}{[A]}$	$\mathrm{m^2\,s^{-1}}$
L	Dimensionless conserved-quantity jump factor, $\frac{[A]}{A'_u \Delta u}$	–
v_a	Advection velocity in the fixed-domain transport equation	$\mathrm{m\,s^{-1}}$
k_{eq}	Equilibrium partition coefficient	–

https://doi.org/10.5194/egusphere-2026-4987
Preprint. Discussion started: 1 September 2026

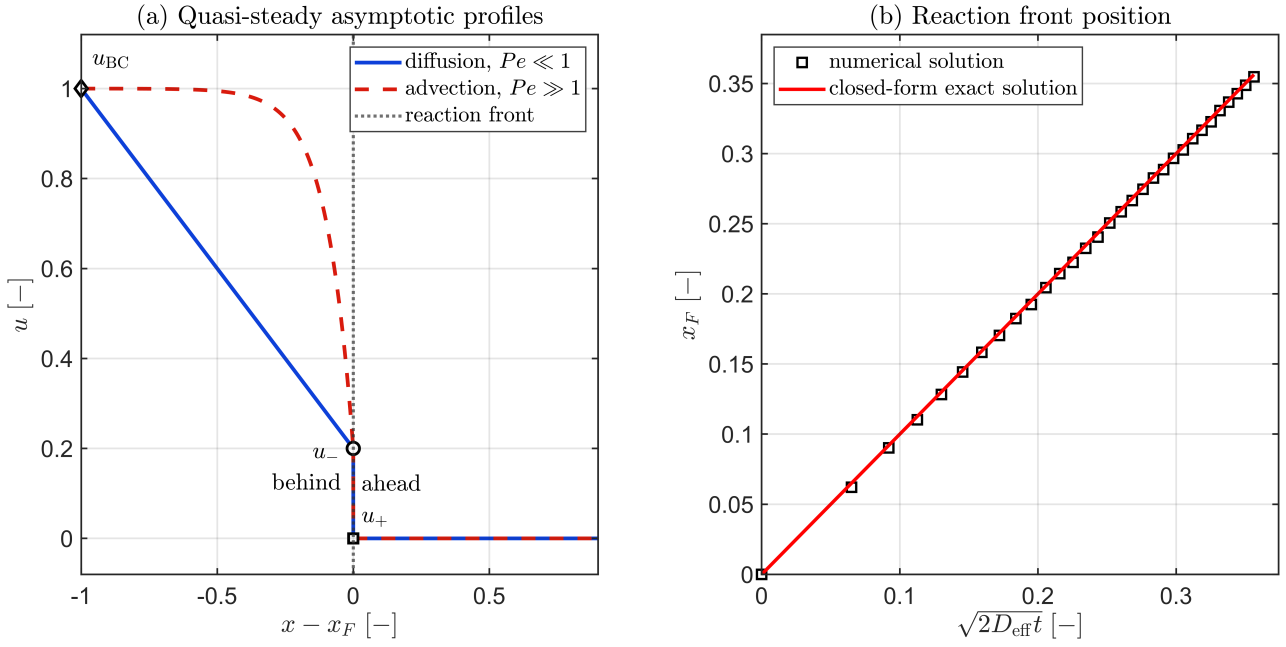

Figure 4. (a) Asymptotic profiles of the scalar field $u(x)$ near a reaction front at $x = x_F$. In the diffusion-dominated limit ($Pe \ll 1$), the profile behind the front is approximately linear, whereas in the advection-dominated limit ($Pe \gg 1$), it forms an exponential boundary layer of thickness $\delta = D/v_a$. Ahead of the front, u is approximately constant. The one-sided values satisfy $u_- = k_{\text{eq}} u_+$; thermodynamic potentials are continuous ($k_{\text{eq}} = 1$), whereas other variables may exhibit a finite jump ($k_{\text{eq}} \neq 1$). (b) Numerical and analytical reaction-front propagation in the diffusion-dominated limit. The analytical solution, $x_F = \sqrt{2D_{\text{eff}}t}$, is linear when plotted against $\sqrt{D_{\text{eff}}t}$, where $D_{\text{eff}} = K\Delta u/[A]$ (see text for details). The numerical conservative solution follows the same $\sqrt{t}$ scaling, demonstrating that D_{eff} combines diffusive transport with the conserved-quantity jump across the moving front.

2.3 Conservation across moving boundary and jump condition

The front velocity follows from conservation across the moving interface. As the front advances, one local equilibrium state replaces another, requiring a finite amount of the conserved quantity to be supplied, removed, or redistributed. The front velocity is therefore determined by balancing the diffusive flux imbalance at the interface with the jump in the conserved quantity between the two equilibrium states (Fig. 5).

We denote by A the relevant conserved quantity per unit bulk volume, representing, depending on the process, internal energy density, total mass density, or mobile-component mass density. Because A depends on u we also sometimes write $A(u)$ to make this dependence clear. Its one-sided values are evaluated at the moving interface, and the jump $[A] = A_- - A_+$ quantifies the finite change in the conserved quantity associated with transformation from one equilibrium state to the other as the front advances.

In the classical Stefan problem, u is temperature and $A(u)$ is internal energy density, with $[A]$ representing the latent heat per unit volume absorbed during melting or released during crystallization. For pressure- and composition-driven reactions, the

https://doi.org/10.5194/egusphere-2026-4987
Preprint. Discussion started: 1 September 2026

physical meaning of $A(u)$ changes, but its mathematical role remains the same: its jump across the front enters the conservation condition that determines the front velocity.

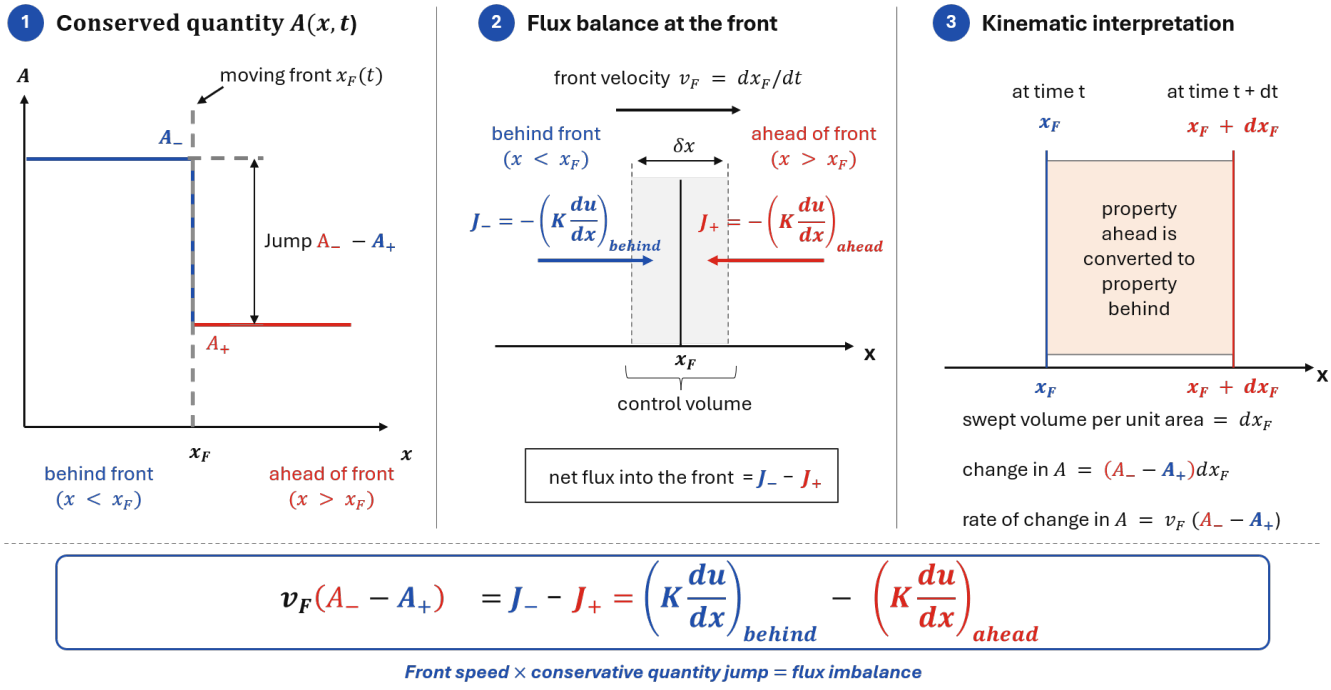

Figure 5. Schematic interpretation of the Stefan–Rankine–Hugoniot jump condition for a moving reaction front. The conserved quantity A has one-sided values A_- behind and A_+ ahead of the front, defining the jump $[A] = A_- - A_+$. As the front advances with velocity $v_F = dx_F/dt$, material ahead of the front is transformed into material behind it, requiring a rate $v_F[A]$ of conserved quantity per unit area. This rate is balanced by the diffusive flux imbalance across the interface according to Eq. (6). In the classical Stefan problem, A is internal energy density and $[A]$ represents latent heat per unit volume. The same structure applies to pressure- and composition-driven reactions with the corresponding conserved quantities.

Conservation at the moving interface gives the Rankine–Hugoniot, or Stefan-type, condition (LeVeque, 2002):

$$[A]\frac{dx_F}{dt} = -\left[K\frac{\partial u}{\partial x}\right]. \tag{6}$$

Here, K is the conductivity associated with diffusive transport. Since the physical diffusive flux is $J = -K\,\partial u/\partial x$, Eq. (6) is equivalently written as $v_F[A] = [J]$ using the jump convention defined above. Thus, the right-hand side of Eq. (6) represents the imbalance of physical diffusive fluxes on the two sides of the front, whereas the left-hand side represents the rate at which the conserved quantity changes as the interface moves. A detailed derivation of the jump condition is given in Appendix B; see Eqs. (B1)–(B7).

https://doi.org/10.5194/egusphere-2026-4987
Preprint. Discussion started: 1 September 2026

In the diffusion-dominated limit, the profile of u behind the front is approximately linear and the flux ahead of the front is zero since u is assumed constant there. Under these assumptions, the jump condition reduces to

$$[A]\,\frac{dx_F}{dt} = K\frac{\Delta u}{x_F(t)}. \tag{7}$$

where, $\Delta u = u_{\mathrm{BC}} - u_-$ is the driving-field contrast across the reacted domain behind the front, defined as the difference between the imposed boundary value u_{BC} and the one-sided value u_- at the reaction front (Fig. 4a). The conductivity K is the value used to evaluate the diffusive flux in the reacted domain.

Equation (7) represents the minimal moving-front law of our derivation. It shows explicitly that the front velocity depends on two factors: the diffusive supply of the transported field u and the jump in conserved quantity across the reaction boundary.

2.4 General explicit propagation law

Equation (7) can be integrated directly when the material properties and the imposed difference in u are constant (see Appendix B for details of the derivation). This yields the characteristic square-root-of-time propagation law for the front position, $x_F(t)$ (Fig. 4b), and velocity, $v_F(t)$:

$$x_F = \sqrt{2D_{\mathrm{eff}}t}, \quad v_F = \sqrt{\frac{D_{\mathrm{eff}}}{2t}}. \tag{8}$$

where D_{eff} is the effective front-propagation diffusivity given by

$$D_{\mathrm{eff}} = \frac{K\,\Delta u}{[A]}. \tag{9}$$

The effective diffusivity D_{eff} generally differs from the transport diffusivity governing the field u, as discussed further below.

The quantities x_F, v_F and D_{eff} apply to temperature–, pressure–, and composition–driven fronts by specifying the transported field u, the conserved quantity per unit bulk volume A, and the transport coefficient K. The corresponding local thermodynamic response, $A'_u = dA/du$, is used further below. Despite their different physical interpretations, these quantities enter the transport equation and moving-boundary condition in the same mathematical form. Throughout the general derivation, the symbol u denotes a generic transported field. In the temperature-driven formulation, $u = T$, whereas $\bar{u}$, u^f, and u^s denote the bulk, fluid, and solid specific internal energies, respectively. The corresponding definitions are summarized as (see Table 2 for explanation of process–specific symbols):

$$u = \begin{pmatrix} T \\ P^f \\ c^f \end{pmatrix}, \qquad A = \begin{pmatrix} \bar{\rho}\bar{u} \\ \bar{\rho} \\ \bar{\rho}\bar{c} \end{pmatrix}, \qquad \frac{dA}{du} = A'_u = \begin{pmatrix} \bar{\rho}\bar{c_p} \\ \bar{\rho}\bar{\beta} \\ \partial\bar{\rho}\bar{c}/\partial c^f \end{pmatrix}, \qquad K = \begin{pmatrix} \bar{\lambda} \\ \rho^f k/\eta^f \\ \varphi\rho^f D_c \end{pmatrix}. \tag{10}$$

The first, second, and third entries in each vector correspond to temperature–, pressure–, and composition–driven fronts, respectively. Here, T denotes temperature, P^f pore-fluid pressure, and c^f the concentration or mass fraction of a mobile chemical component in the fluid. The conserved quantity A represents the corresponding extensive quantity per unit bulk volume. For

https://doi.org/10.5194/egusphere-2026-4987
Preprint. Discussion started: 1 September 2026

temperature-driven fronts, $A = \bar{\rho}\bar{u}$ is the bulk internal energy density; for pressure-driven fronts, $A = \bar{\rho}$ is the total mass density of the fluid–solid mixture; and for composition-driven fronts, $A = \bar{\rho}\bar{c}$ is the total mass density of the mobile component, including its storage in both fluid and solid phases.

2.5 The dimensionless number L controlling propagation of reactions

The effective diffusivity of a propagating reaction front can be expressed by separating diffusive transport from the effect of the finite jump in the conserved quantity across the front. This distinction reflects the different roles of the transported field u and the conserved quantity A: the gradient of u drives the diffusive flux, whereas the jump in A quantifies the amount of conserved quantity that must be supplied, removed, or redistributed as the front advances.

We introduce the dimensionless L number that can be applied to temperature-, pressure- and composition-driven reaction fronts:

$$L = \frac{[A]}{A'_u \, \Delta u}, \tag{11}$$

The L number in (11) can be interpreted as follows: the numerator, $[A]$, represents the finite change in A across the reaction front due to the reaction, whereas the denominator, $A'_u \Delta u$, represents the local change in A associated with the variation in u within the reacted region behind the front.

The effective diffusivity for reaction front propagation can be expressed with L:

$$D_{\text{eff}} = \frac{K \, \Delta u}{[A]} = \frac{D}{L}, \tag{12}$$

whereby,

$$D = \frac{K}{A'_u}. \tag{13}$$

The coefficient D is the transport diffusivity of the transported field in the reacted domain behind the advancing front.

The physically relevant reaction front propagation regime considered here corresponds to $L > 1$. In this case, the finite amount of conserved quantity A that must be supplied, removed, or redistributed in order to advance the front is larger than the estimate $A'_u \Delta u$. Since $D_{\text{eff}} = D/L$, this gives $D_{\text{eff}} < D$, and the front propagates more slowly than would be inferred from the transport diffusivity D alone. If $L \approx 1$, D_{eff} approaches D, and the moving-front law reduces to the standard diffusion-controlled scaling.

3 Common structure of the solution for temperature-, pressure-, and composition-driven reaction fronts

3.1 Driving potentials u and conserved quantities A

We distinguish between the transported potential u and the conserved quantity A that depends on u. The potential u, such as temperature, fluid pressure, or chemical potential, drives the diffusive flux and is assumed to be continuous across the

https://doi.org/10.5194/egusphere-2026-4987
Preprint. Discussion started: 1 September 2026

Table 2. Notation and shorthand definitions used throughout the manuscript.

Symbol	Meaning	Unit
^{f}	Superscript indicating that the quantity refers to the fluid phase	–
^{s}	Superscript indicating that the quantity refers to the solid phase	–
T	Temperature, $T^f = T^s = T$	K
P^f, P^s	Fluid and solid pressure	Pa
c^f, c^s	Concentration of the component in the fluid and solid phase	–
$c^f_{SiO_2}$, $c^s_{SiO_2}$	Concentration of volatile SiO_2 in the fluid and solid phase	–
φ	Porosity	–
ρ^f, ρ^s	Fluid and solid densities	$\mathrm{kg\,m^{-3}}$
u^f, u^s	Fluid and solid specific internal energies	$\mathrm{J\,kg^{-1}}$
λ^f, λ^s	Fluid and solid thermal conductivities	$\mathrm{W\,m^{-1}\,K^{-1}}$
c^f_p, c^s_p	Fluid and solid thermal capacities	$\mathrm{J\,kg^{-1}\,K^{-1}}$
k	Permeability	$\mathrm{m^2}$
η^f	Fluid viscosity	$\mathrm{Pa\,s}$
D_c	True diffusivity of the volatile component	$\mathrm{m^2\,s^{-1}}$
$\bar{\rho}$	Total density, $\varphi\rho^f + (1-\varphi)\rho^s$	$\mathrm{kg\,m^{-3}}$
$\bar{u}$	Specific internal energy, $\left(\varphi\rho^f u^f + (1-\varphi)\rho^s u^s\right)/\bar{\rho}$	$\mathrm{J\,kg^{-1}}$
$\bar{c}$	Total mobile-component mass concentration, $\left(\varphi\rho^f c^f + (1-\varphi)\rho^s c^s\right)/\bar{\rho}$	$\mathrm{kg\,kg^{-1}}$
$\bar{c}_{SiO_2}$	Total mass concentration of SiO_2	$\mathrm{kg\,kg^{-1}}$
$\bar{c}_p$	Effective specific heat capacity, $\varphi c^f_p + (1-\varphi)c^s_p$	$\mathrm{J\,kg^{-1}\,K^{-1}}$
$\bar{\lambda}$	Effective thermal conductivity, $\varphi\lambda^f + (1-\varphi)\lambda^s$	$\mathrm{W\,m^{-1}\,K^{-1}}$
β^f, β^s	Fluid and solid compressibilities, $\beta^f = \frac{1}{\rho^f}\frac{d\rho^f}{dP^f}$ and $\beta^s = \frac{1}{\rho^s}\frac{d\rho^s}{dP^s}$	$\mathrm{Pa^{-1}}$
β_φ	Pore compressibility, $\frac{d\varphi}{dP^f}$	$\mathrm{Pa^{-1}}$
$\bar{\beta}$	Effective compressibility, $\bar{\beta} = \frac{1}{\bar{\rho}}\frac{d\bar{\rho}}{dP^f} = \frac{1}{\bar{\rho}}\left[\varphi\rho^f\beta^f + (1-\varphi)\rho^s\beta^s\frac{dP^s}{dP^f} + (\rho^f - \rho^s)\beta_\varphi\right]$	$\mathrm{Pa^{-1}}$

https://doi.org/10.5194/egusphere-2026-4987
Preprint. Discussion started: 1 September 2026

moving front in the diffusion-controlled limit. In contrast, A represents the conserved quantity per unit bulk volume, such as internal energy, total mass, or total component mass, and may have different equilibrium values on both sides of the front. The associated thermodynamic transformation may also produce discontinuous changes in non-conserved state variables, such as phase fractions and porosity. Thus, $A(u)$ depends on u and may exhibit a finite jump across the reaction front even though the driving potential u remains continuous. The one-dimensional conservative transport equation is then written as

$$\frac{\partial A(u)}{\partial t} - \frac{\partial}{\partial x}\left(K(u)\frac{\partial u}{\partial x}\right) = 0, \tag{14}$$

where $K(u)$ is the conductivity associated with transport of u. This equation combines the thermodynamic potential u, which controls the flux, with the conserved quantity $A(u)$. The separation between u and $A(u)$ is the key structure of our general approach. To use Eq. (14) in a practical problem, the relation between u and $A(u)$ must be closed thermodynamically.

3.2 Piecewise topology of thermodynamic u–A relation

The thermodynamic closure between u and A specifies the amount of the conserved quantity stored per unit bulk volume for the local equilibrium state defined by u. The thermodynamic relation between the transported field u and the conserved quantity A is hereafter referred to as the u–A relation. The physical meaning of the u–A relation depends on the process considered (see Eq. (10)). For practical applications, the closure relation A is obtained from equilibrium thermodynamic calculations, which determine the stable assemblage and corresponding conserved quantity as a function of u. Figure 6 shows examples calculated with ThermoLab (Vrijmoed and Podladchikov, 2022) at fixed external conditions. For the brucite–periclase–water system, $u = P^f$ and $A = \bar{\rho}$. For the brucite–antigorite–forsterite–water system, $u = c^f$ and $A = \bar{\rho}\bar{c}$.

The topology of the u–A relation is central to the formulation. Figure 6 shows this relation for the pairs P^f–$\bar{\rho}$ and c^f–$\bar{\rho}\bar{c}$, which play the same mathematical role as T–$\bar{\rho}\bar{u}$ in the classical thermal Stefan problem. Along a smooth equilibrium branch, A is single-valued and differentiable, such that $A'_u = \partial A/\partial u$ is well defined. Equation (14) can then be reduced locally to a standard diffusion or advection–diffusion equation for u, with A'_u representing the local thermodynamic response. The differential formulation is therefore valid within smooth equilibrium branches, away from the reaction.

At a reaction, however, the thermodynamic relation may contain a kink or a horizontal or nearly horizontal segment, along which u is buffered while A changes by a finite amount due to the reaction. In the limiting case of perfect buffering, A becomes multivalued at the reaction value of u, and the local derivative A'_u cannot represent the finite change in A. The reaction must therefore be treated as a moving interface whose evolution is governed by the jump condition (6).

https://doi.org/10.5194/egusphere-2026-4987
Preprint. Discussion started: 1 September 2026

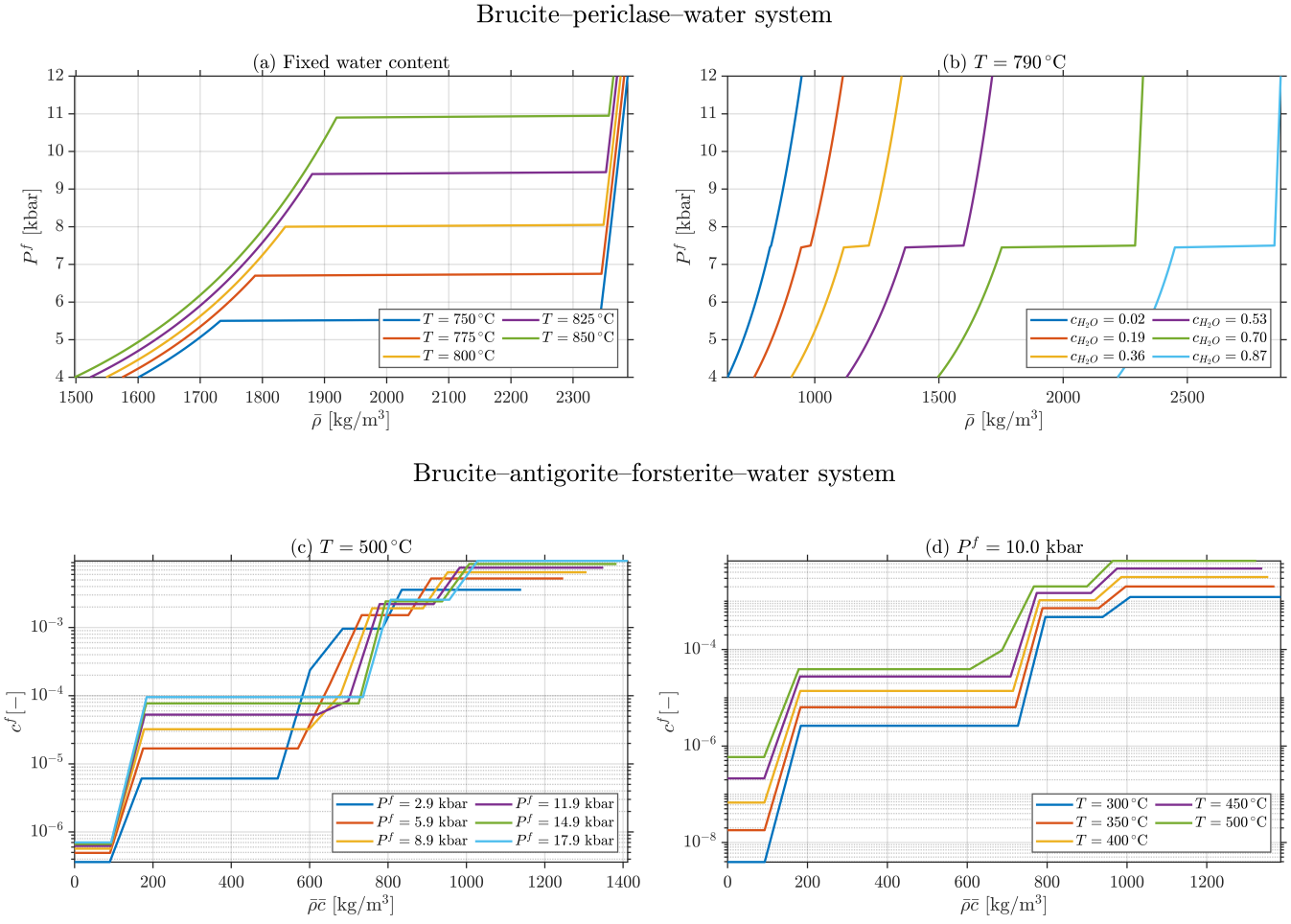

Figure 6. Thermodynamic u–A relations for pressure- and composition-driven reaction fronts obtained from equilibrium thermodynamic calculations. Horizontal axes show the conserved quantity per unit bulk volume, A, and vertical axes the transported field, u. (a,b) Brucite–periclase–water system with $u = P^f$ and $A = \bar{\rho}$. Panel (a) shows P^f–$\bar{\rho}$ relations at fixed water content for different temperatures, and (b) at $T = 790\,^\circ$C for different water contents, c_{H_2O}. (c,d) Brucite–antigorite–forsterite–water system with $u = c^f$ and $A = \bar{\rho}\bar{c}$. Panel (c) shows c^f–$\bar{\rho}\bar{c}$ relations at $T = 500\,^\circ$C for different fluid pressures, P^f, and (d) at $P^f = 10.0$ kbar for different temperatures. Changes in slope and horizontal or nearly horizontal segments reflect reaction thresholds and changes in stable mineral assemblage, across which the conserved quantity may change by a finite amount.

To obtain a general analytical formulation, we approximate the thermodynamic closure by a piecewise-linear relation, as illustrated in Fig. 7. Each linear segment represents a smooth equilibrium branch with constant $A'u$, whereas the reaction front represents the transition between two branches. The corresponding one-sided values, $A-$ and A_+, are determined from thermodynamic equilibrium calculations.

https://doi.org/10.5194/egusphere-2026-4987
Preprint. Discussion started: 1 September 2026

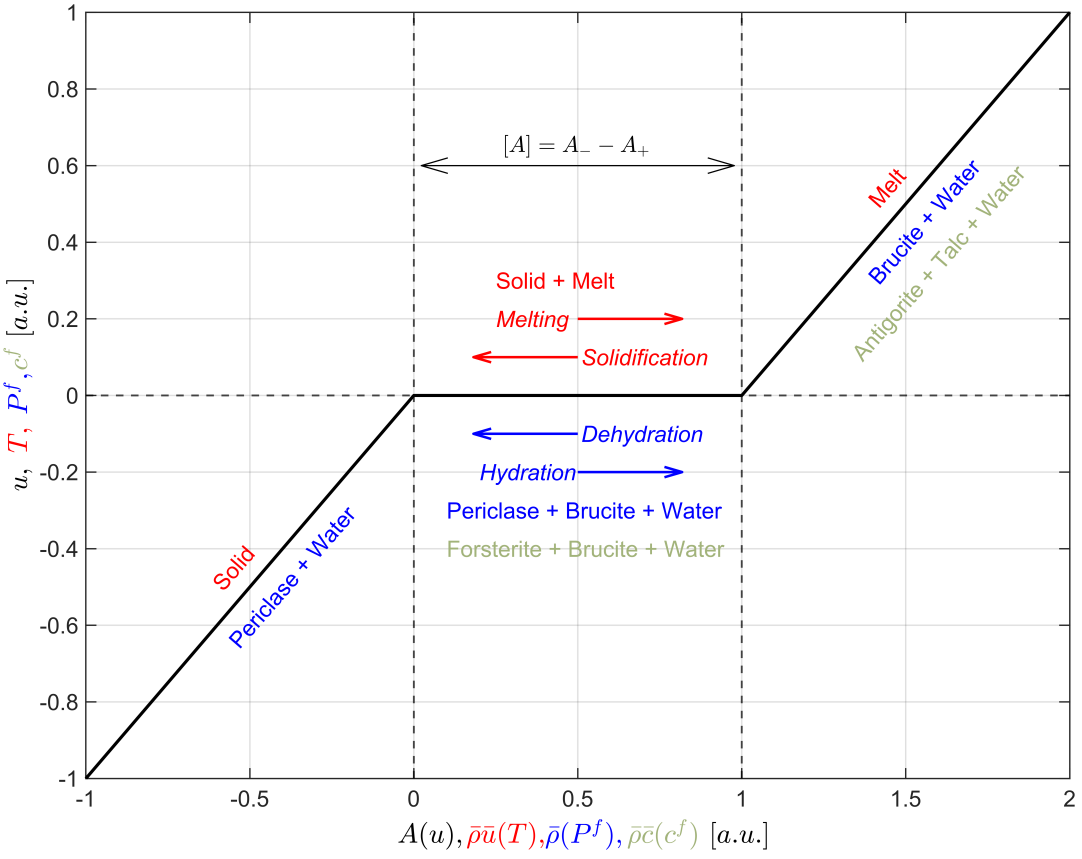

Figure 7. Schematic thermodynamic u–A relation underlying the moving-boundary formulation, where u represents temperature, pressure, or composition and A the corresponding conserved quantity per unit bulk volume. In applications, the u–A relation is obtained from equilibrium thermodynamic calculations and approximated as piecewise linear. Along smooth equilibrium branches, $A'_u = \partial A/\partial u$ is well defined and governs local storage. At a reaction threshold, u may be buffered while A changes by a finite amount, requiring a moving-interface description in which the conserved-quantity jump $[A]$ controls front propagation.

3.3 Temperature-, pressure-, and composition-driven reaction fronts

Temperature-, pressure-, and composition-driven reaction fronts share the same mathematical structure: a conservative transport equation, Eq. (14), closed by a piecewise-linear thermodynamic u–A relation and supplemented by the jump condition at the reaction interface, Eq. (6). This formulation applies to all three driving mechanisms; only the physical definitions of u, A, and K differ between them. The common structure is illustrated in Fig. 7 and summarized in Table 3, which lists the corresponding quantities and parameters.

https://doi.org/10.5194/egusphere-2026-4987
Preprint. Discussion started: 1 September 2026

Table 3. Summary of the unified quasi-steady Stefan-like solution for temperature-, pressure-, and composition-driven reaction fronts. For each driving field u, the conserved quantity A, its local derivative A'_u behind the front, and the transport coefficient K define the transport diffusivity $D = K/A'_u$. The front position is $x_F(t) = \sqrt{2D_{\mathrm{eff}}t}$, with effective front diffusivity $D_{\mathrm{eff}} = D/L$ and $L = [A]/(A'_u\Delta u)$. The dimensionless L number compares the conserved-quantity jump across the reaction front with the corresponding continuous storage change associated with the driving-field contrast Δu. For temperature-driven fronts, L is the inverse of the classical Stefan number.

Driving mechanism	u	A	$A'_u = \frac{dA}{du}$	K	$D = \frac{K}{A'_u}$	$L = \frac{[A]}{A'_u\,\Delta u}$	$D_{\mathrm{eff}} = \frac{D}{L}$
Temperature	T	$\bar{\rho}\bar{u}$	$\bar{\rho}\bar{c_p}$	$\bar{\lambda}$	$\frac{\bar{\lambda}}{\bar{\rho}\bar{c_p}}$	$\frac{[\bar{\rho}\bar{u}]}{\bar{\rho}\bar{c_p}\,\Delta T}$	$\bar{\lambda}\frac{\Delta T}{[\bar{\rho}\bar{u}]}$
Pressure	P^f	$\bar{\rho}$	$\bar{\rho}\bar{\beta}$	$\frac{\rho^f\,k(\varphi)}{\eta^f}$	$\frac{\rho^f\,k(\varphi)}{\eta^f\,\bar{\rho}\bar{\beta}}$	$\frac{[\bar{\rho}]}{\bar{\rho}\bar{\beta}\,\Delta P^f}$	$\frac{k(\varphi)}{\eta^f}\frac{\rho^f\,\Delta P^f}{[\bar{\rho}]}$
Composition	c^f	$\bar{\rho}\bar{c}$	$\frac{\partial\bar{\rho}\bar{c}}{\partial c^f}$	$\varphi\rho^f D_c$	$\frac{\varphi\rho^f D_c}{\partial\bar{\rho}\bar{c}/\partial c^f}$	$\frac{[\bar{\rho}\bar{c}]}{\partial\bar{\rho}\bar{c}/\partial c^f\,\Delta c^f}$	$D_c\frac{\varphi\rho^f\,\Delta c^f}{[\bar{\rho}\bar{c}]}$

4 Applications to pressure- and composition-driven reaction fronts

We apply the analytical solution derived in sections 2–3 to two specific mineral reactions by assigning the process-specific transported field u, conserved quantity A, local derivative A'_u, and transport coefficient K, following Eq. (10) and Table 3. The reaction-front position then follows directly from the propagation law in Eqs. (8)–(12). Each application therefore requires the thermodynamic u–A relation, the driving-field contrast, and the relevant transport parameters.

We consider two representative cases: pressure-driven hydration in the brucite–periclase system and composition-driven hydration in the brucite–antigorite–forsterite–talc–quartz system. These examples involve different transported fields and conserved quantities but share the same moving-boundary structure. For the pressure-driven case, $u = P^f$ and $A = \bar{\rho}$, whereas for the composition-driven case, $u = c^f_{\mathrm{SiO_2}}$ and $A = \bar{\rho}\bar{c}_{\mathrm{SiO_2}}$. The corresponding thermodynamic u–A relations, hereafter referred to as lookup tables, are calculated with ThermoLab (Vrijmoed and Podladchikov, 2022) and shown in Figure 8. The pressure-driven example involves a density jump across the brucite–periclase reaction threshold, whereas the composition-driven example involves a jump in total silica mass across an assemblage change. Despite these different physical meanings of u and A, both examples follow the same mathematical formulation.

Figure 8 also indicates the initial and boundary values of u and A. The initial values represent the uniform ambient equilibrium state ahead of the reaction front (Fig. 4a). In both examples, the imposed boundary value of u exceeds its initial value, generating a gradient that drives diffusive transport toward the reaction front. The difference between the boundary and initial values defines the driving-field contrast Δu.

For the analytical solution, the thermodynamic lookup tables are approximated by piecewise-linear u–A relations with the topology introduced in section 3.2. These relations provide the local derivative A'_u and the one-sided equilibrium values A_- and A_+, from which the jump $[A]$ is obtained according to the general structure shown in Figure 7. Together with Δu, these

https://doi.org/10.5194/egusphere-2026-4987
Preprint. Discussion started: 1 September 2026

quantities determine the thermodynamic contribution to the front-propagation law. The remaining transport parameters, such as permeability or chemical transport diffusivity, are specified in the following two sections for each application.

To test the approximations underlying the explicit analytical solution, we perform one-dimensional (1D) numerical simulations for both examples using the same initial and boundary conditions. The conservative transport equation, Eq. (14), is solved for A using finite differences and explicit time integration, similar to the open-access numerical algorithm of Schmalholz et al. (2024) for (de)hydration-front propagation. After each time step, the calculated values of A are converted to the corresponding values of u using the thermodynamic relations shown in Figure 8. Unlike the analytical solution, the numerical simulations use the original ThermoLab lookup tables rather than their piecewise-linear approximations, with u obtained by numerical interpolation from A.

The numerical simulations involve fewer simplifications than the analytical solution. In particular, they resolve the transient evolution of the transported field rather than assuming a quasi-steady state, calculate the spatial profile of u rather than assuming a linear profile behind the front, and allow nonlinear transport parameters to vary in space and time. For example, the pressure-driven simulation presented in the next section accounts for porosity-dependent permeability. The numerical simulations therefore provide a test of the approximations underlying the explicit analytical solution for the evolution of the reaction-front position, $x_F(t)$.

https://doi.org/10.5194/egusphere-2026-4987
Preprint. Discussion started: 1 September 2026

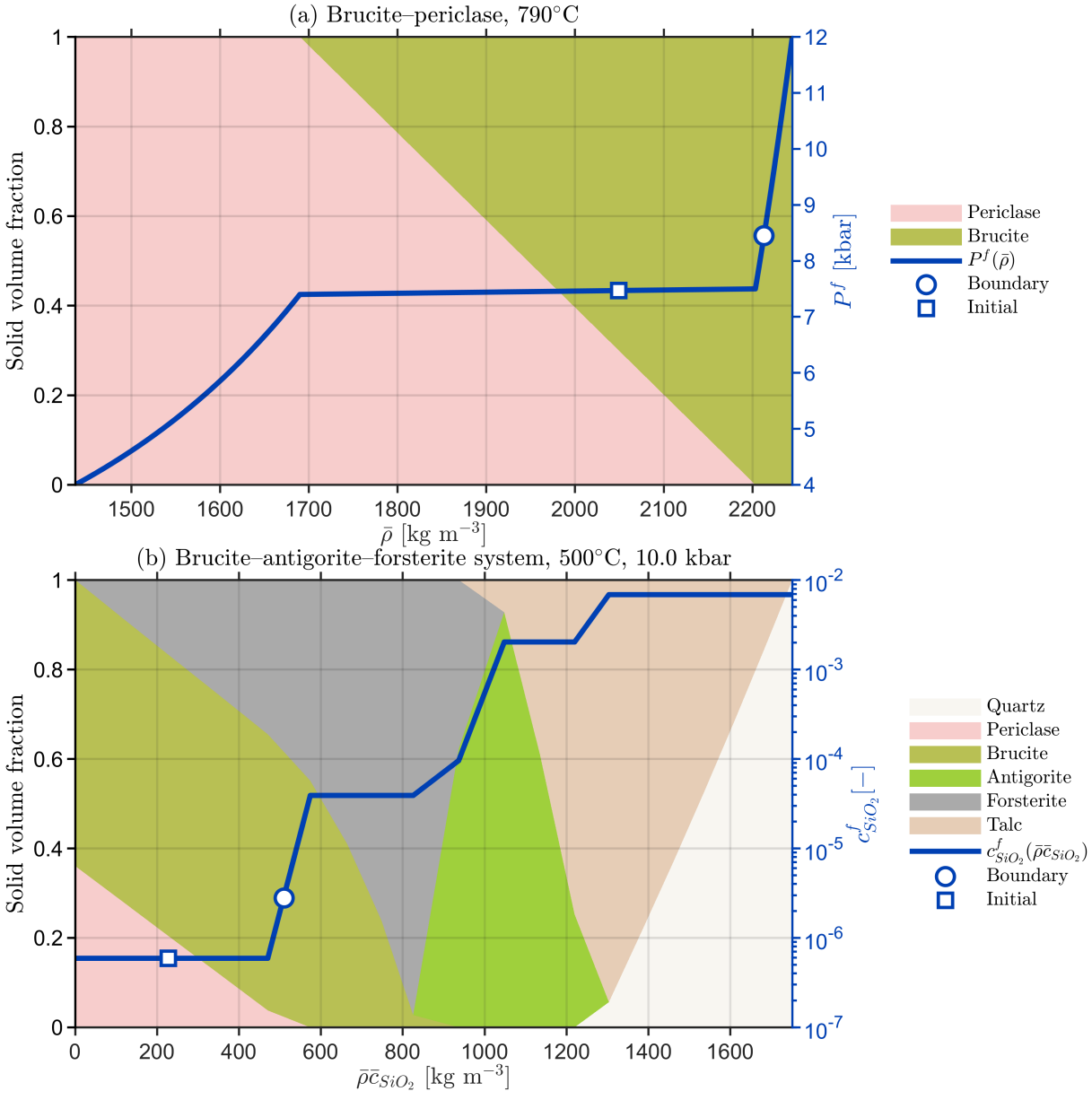

Figure 8. Thermodynamic u–A relations used for the two applications, calculated with ThermoLab (Vrijmoed and Podladchikov, 2022). (a) Pressure-driven brucite–periclase hydration at 790 °C, with $u = P^f$ and $A = \bar{\rho}$. Colored regions show equilibrium mineral fractions and the blue curve the P^f–$\bar{\rho}$ relation. (b) Composition-driven hydration in the periclase–brucite–antigorite–forsterite–talc–quartz–water system at 500 °C and 10.0 kbar, with $u = c^f_{\mathrm{SiO_2}}$ and $A = \bar{\rho}\bar{c}\mathrm{SiO_2}$. Colored regions show equilibrium mineral fractions and the blue curve the $c^f\,\mathrm{SiO_2}$–$\bar{\rho}\bar{c}_{\mathrm{SiO_2}}$ relation on a logarithmic scale. Squares and circles mark the initial and boundary values, respectively, used in the numerical simulation. In both cases, reaction-induced changes in mineral assemblage produce the finite jump in A governing front propagation.

https://doi.org/10.5194/egusphere-2026-4987
Preprint. Discussion started: 1 September 2026

4.1 Pressure-driven hydration in the brucite–periclase system

We consider pressure-driven hydration in the brucite–periclase–water system at $T = 790\,^{\circ}\mathrm{C}$ (Schmalholz et al., 2020). The reaction is

$$\mathrm{MgO} + \mathrm{H_2O} \rightleftharpoons \mathrm{Mg(OH)_2}. \tag{15}$$

Using $u = P^f$ and $A = \bar{\rho}$, the governing conservation equation is

$$\frac{\partial \bar{\rho}}{\partial t} - \frac{\partial}{\partial x}\left(\rho^f \frac{k_0 \phi^n}{\eta^f} \frac{\partial P^f}{\partial x}\right) = 0, \tag{16}$$

where $k(\phi) = k_0 \phi^n$ is the permeability, k_0 a reference permeability, ϕ the porosity, n an exponent and η^f the fluid viscosity.

The system of equations is closed by the thermodynamic equilibrium relation $\bar{\rho}$–P^f, calculated with ThermoLab (Vrijmoed and Podladchikov, 2022) using the thermodynamic database of Holland and Powell (1998) (Fig. 8a). The nearly pressure-buffered segment at approximately 7.5 kbar corresponds to progressive replacement of periclase by brucite.

The 1D domain has length $L_c = 1$ m and an initial pressure $P^f_{\mathrm{ini}} = 7.47$ kbar. Hydration is initiated by imposing $P^f_{\mathrm{BC}} = 8.45$ kbar at the left boundary. The pressure difference to be used in the analytical estimate is then

$$\Delta P^f = P^f_{\mathrm{BC}} - P^f_{\mathrm{ini}} \simeq 0.98 \times 10^8 \ \mathrm{Pa}. \tag{17}$$

We apply an initial porosity in the periclase of $\phi = 0.272$, which reduces to $\phi = 0.0423$ in the brucite after the hydration. This reduced porosity is used in the calculation of the permeability. Across the reaction interval, the total density increases from $\bar{\rho}_+ = 2049\ \mathrm{kg\,m^{-3}}$ ahead of the front to $\bar{\rho}_- \simeq 2200\ \mathrm{kg\,m^{-3}}$ behind it. The jump in the conserved quantity is then,

$$[\bar{\rho}] = \bar{\rho}_- - \bar{\rho}_+ \simeq 151\ \mathrm{kg\,m^{-3}}. \tag{18}$$

We further apply the representative parameters $\rho^f = 838\ \mathrm{kg\,m^{-3}}$ and $\bar{\beta} = 1.27 \times 10^{-10}\ \mathrm{Pa^{-1}}$. Here,

$$\bar{\beta} = \frac{1}{\bar{\rho}} \frac{d\bar{\rho}}{dP^f} \tag{19}$$

is the effective compressibility obtained from the local slope of the thermodynamic $\bar{\rho}$–(P^f) relation. The permeability law uses $k_0/\eta^f = 10^{-12}\ \mathrm{m^2\,Pa^{-1}\,s^{-1}}$ and $n = 3$. For the pressure-driven problem, the derivative A'_u and transport coefficient are

$$A'_{P^f} = \frac{d\bar{\rho}}{dP^f} = \bar{\rho}\bar{\beta}, \qquad K = \rho^f \frac{k_0 \phi^n}{\eta^f}. \tag{20}$$

Taking $\bar{\rho} \simeq \bar{\rho}_- = 2200\ \mathrm{kg\,m^{-3}}$ as representative value in the reacted domain, the corresponding hydraulic diffusivity is

$$D = \frac{K}{A'_{P^f}} = \frac{\rho^f k_0 \phi^n}{\eta^f \bar{\rho}\bar{\beta}} \simeq 2.27 \times 10^{-7}\ \mathrm{m^2\,s^{-1}}. \tag{21}$$

The L number is

$$L = \frac{[\bar{\rho}]}{\bar{\rho}\bar{\beta}\Delta P^f} \simeq 5.51. \tag{22}$$

https://doi.org/10.5194/egusphere-2026-4987
Preprint. Discussion started: 1 September 2026

Consequently, the effective diffusivity is

$$D_{\text{eff}} = \frac{D}{L} = \frac{\rho^f k_0 \phi^n}{\eta^f} \frac{\Delta P^f}{[\bar{\rho}]} \simeq 4.12 \times 10^{-8}\ \text{m}^2\,\text{s}^{-1}. \tag{23}$$

Figure 9 shows the numerically calculated spatial profiles of P^f and $\bar{\rho}$ at a representative simulation time and compares the numerical reaction-front position with the explicit analytical prediction. The numerical solution exhibits an approximately linear P^f profile behind the front, consistent with the assumption of the analytical solution, and a sharp jump in $\bar{\rho}$ across the reaction front. The numerical front position was determined at each time step as the furthest position from the left model boundary where the absolute value of the spatial gradient of P^f exceeded a small threshold, $|\partial P^f/\partial x| > 10^{-3}$, because the spatial gradient is zero ahead of the reaction front. The resulting front position is plotted against the square root of time in Figure 9d. The analytical front position is calculated from Eq. (8) using the effective diffusivity given by Eq. (23). The analytical and numerical predictions of $x_F(t)$ are in close agreement.

https://doi.org/10.5194/egusphere-2026-4987
Preprint. Discussion started: 1 September 2026

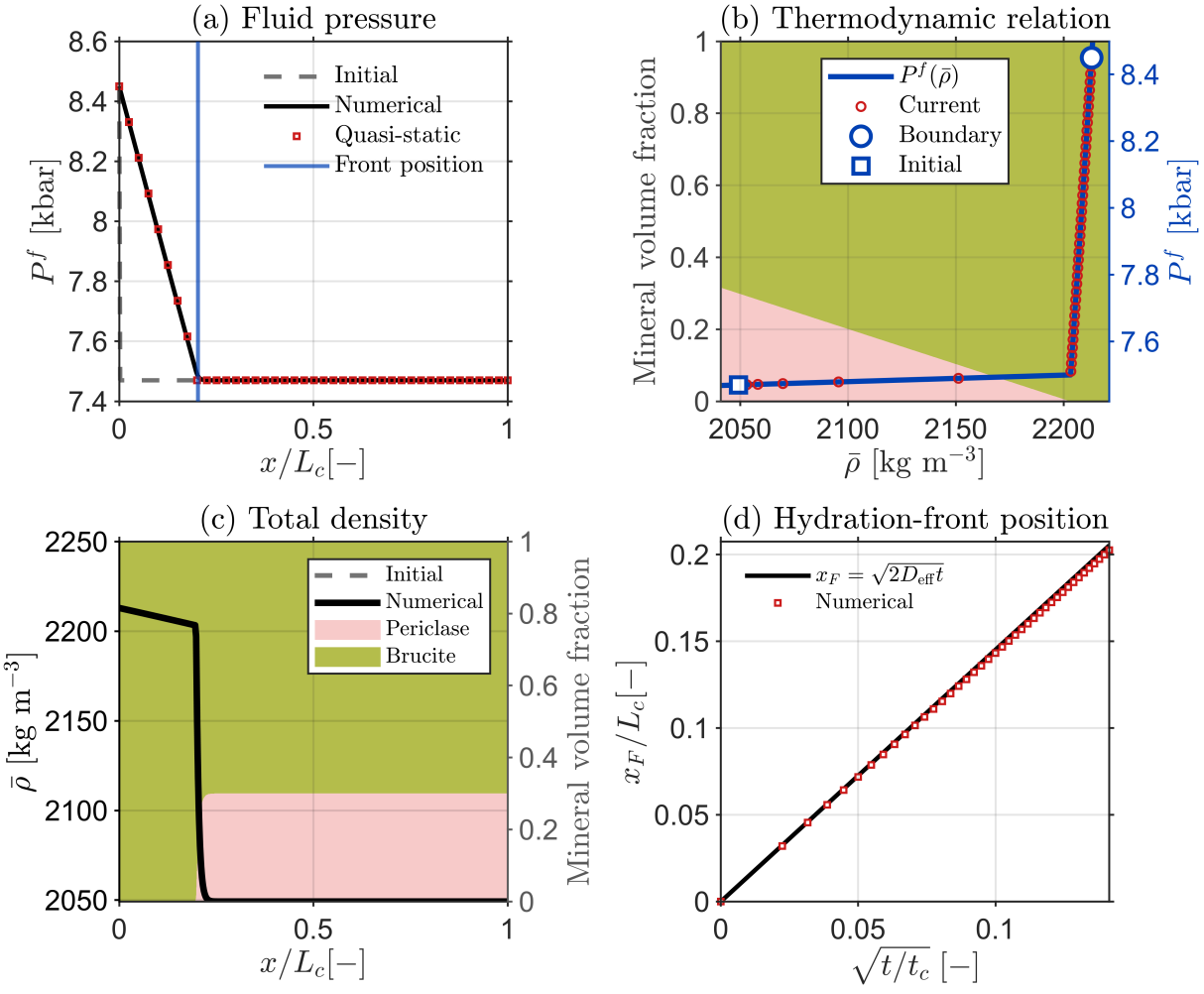

Figure 9. Numerical simulation of pressure-driven periclase hydration front and analytical solution. (a) Fluid-pressure profile $P^f(x,t)$ during hydration of periclase to brucite. The dashed grey curve shows the initial condition, the black curve the numerical solution, and red symbols the analytical solution. (b) Thermodynamic P^f–$\bar{\rho}$ relation at $T = 790\,^\circ\mathrm{C}$ and fixed bulk water content. Colored regions show equilibrium mineral fractions, red symbols the numerical states, and the open circle and square the boundary and initial states, respectively. (c) Total density $\bar{\rho}(x,t)$ and mineral-volume-fraction profiles showing the sharp transition between hydrated and initial material. (d) Reaction-front position versus the square root of normalized time. The red symbols show the numerical solution and the black line shows the analytical prediction $x_F(t) = \sqrt{2D_{\text{eff}}t}$, with $D_{\text{eff}} = D/L$, $D = \rho^f k/(\eta^f \bar{\rho}\bar{\beta})$, and $L = [\bar{\rho}]/(\bar{\rho}\bar{\beta}\Delta P^f)$. Time is normalized by the characteristic front-propagation time $t_c = L_c^2/D_{\text{eff}}$.

4.2 Composition-driven hydration in the brucite–antigorite–forsterite system

We now consider composition-driven hydration in the multicomponent periclase–brucite–antigorite–forsterite–talc–quartz–water system at $T = 500\,^\circ\mathrm{C}$ and $P = 10.0\,\mathrm{kbar}$. The complete thermodynamic system permits several silica-bearing assem-

https://doi.org/10.5194/egusphere-2026-4987
Preprint. Discussion started: 1 September 2026

blages. However, the low-silica interval selected for the transport calculation contains only periclase, brucite, and forsterite. It therefore extends the brucite–periclase system considered in section 4.1 by including silica transport and forsterite stability.

For this application, $u = c^f_{\mathrm{SiO_2}}$, which is used as a monotonic proxy for silica chemical potential, and $A = \bar{\rho}\bar{c}_{\mathrm{SiO_2}}$, including silica stored in both the fluid and solid phases. Silica diffuses only through the pore fluid, whereas solid-state diffusion is neglected. The governing conservation equation is

$$\frac{\partial}{\partial t}\left(\bar{\rho}\bar{c}_{\mathrm{SiO_2}}\right) - \frac{\partial}{\partial x}\left(\rho^f \phi D_c \frac{\partial c^f_{\mathrm{SiO_2}}}{\partial x}\right) = 0, \tag{24}$$

where D_c is the pore-fluid diffusivity of dissolved silica and

$$K_c = \rho^f \phi D_c \tag{25}$$

is the corresponding compositional transport coefficient per unit bulk cross-sectional area.

The system of equations is closed with the equilibrium relation $c^f_{\mathrm{SiO_2}}$–$\bar{\rho}\bar{c}_{\mathrm{SiO_2}}$ calculated with ThermoLab (Vrijmoed and Podladchikov, 2022) using the thermodynamic database of Holland and Powell (1998) (Fig. 8b). The thermodynamic relation $c^f_{\mathrm{SiO_2}}$–$\bar{\rho}\bar{c}_{\mathrm{SiO_2}}$ exhibits a low-silica, composition-buffered segment which allows the total silica content to change substantially while the dissolved silica concentration remains nearly constant.

The 1D model domain has a length $L_c = 1\,\mathrm{m}$ and is initially uniform except at the left model boundary. The initial values in the ambient region ahead of the reaction front are

$$\bar{\rho}\bar{c}_{\mathrm{SiO_{2+}}} = 189.503\,\mathrm{kg\,m^{-3}}, \qquad c^f_{\mathrm{SiO_{2+}}} = 5.911 \times 10^{-7}, \tag{26}$$

and the values at the left model boundary are

$$\bar{\rho}\bar{c}_{\mathrm{SiO_{2BC}}} = 510.292\,\mathrm{kg\,m^{-3}}, \qquad c^f_{\mathrm{SiO_{2BC}}} = 2.788 \times 10^{-6}. \tag{27}$$

The imposed concentration gradient transports silica into the domain and shifts the local equilibrium assemblage toward the more silica-rich state. Immediately behind the advancing reaction front,

$$\bar{\rho}\bar{c}_{\mathrm{SiO_{2-}}} = 454.806\,\mathrm{kg\,m^{-3}}, \qquad c^f_{\mathrm{SiO_{2-}}} = 5.911 \times 10^{-7}. \tag{28}$$

The jump in total silica content across the reaction interval is therefore

$$[\bar{\rho}\bar{c}_{\mathrm{SiO_2}}] = \bar{\rho}\bar{c}_{\mathrm{SiO_{2-}}} - \bar{\rho}\bar{c}_{\mathrm{SiO_{2+}}} = 265.304\,\mathrm{kg\,m^{-3}}. \tag{29}$$

The dissolved-silica contrast across the reacted domain is

$$\Delta c^f_{\mathrm{SiO_2}} = c^f_{\mathrm{SiO_{2BC}}} - c^f_{\mathrm{SiO_{2-}}} = 2.197 \times 10^{-6}. \tag{30}$$

The representative boundary-state parameters used for the reacted domain are $\rho^f = 1004.8\,\mathrm{kg\,m^{-3}}$ and $\phi = 0.0229$. The transport calculation uses $D_c = 1.0 \times 10^{-2}\,\mathrm{m^2\,s^{-1}}$, giving

$$K_c = \rho^f \phi D_c \simeq 2.30 \times 10^{-1}\,\mathrm{kg\,m^{-1}\,s^{-1}}. \tag{31}$$

https://doi.org/10.5194/egusphere-2026-4987
Preprint. Discussion started: 1 September 2026

The derivative A'_c is

$$A'_c = \frac{\bar{\rho}\bar{c}_{\mathrm{SiO_2BC}} - \bar{\rho}\bar{c}_{\mathrm{SiO_2-}}}{c^f_{\mathrm{SiO_2BC}} - c^f_{\mathrm{SiO_2-}}} \simeq 2.53 \times 10^7\,\mathrm{kg\,m^{-3}}. \tag{32}$$

The corresponding compositional diffusivity in the reacted domain is therefore

$$D = \frac{K_c}{A'_c} = \frac{\rho^f \phi D_c}{A'_c} \simeq 9.09 \times 10^{-9}\,\mathrm{m^2\,s^{-1}}. \tag{33}$$

The dimensionless L number is

$$L = \frac{[\bar{\rho}\bar{c}_{\mathrm{SiO_2}}]}{A'_c \Delta c^f_{\mathrm{SiO_2}}} \simeq 4.78. \tag{34}$$

Consequently, the effective diffusivity is

$$D_{\mathrm{eff}} = \frac{D}{L} = \frac{\rho^f \phi D_c \Delta c^f_{\mathrm{SiO_2}}}{[\bar{\rho}\bar{c}_{\mathrm{SiO_2}}]} \simeq 1.90 \times 10^{-9}\,\mathrm{m^2\,s^{-1}}. \tag{35}$$

Figure 10 shows the numerically calculated spatial profiles of $c^f_{\mathrm{SiO_2}}$ and $\bar{\rho}\bar{c}_{\mathrm{SiO_2}}$ at a representative simulation time and compares the numerical reaction-front position with the explicit analytical prediction. The analytical and numerical predictions of $x_F(t)$ show good overall agreement, although a small systematic deviation is apparent, unlike for the pressure-driven front in the previous section. Nevertheless, the analytical solution captures the first-order evolution of the composition-driven reaction front.

The deviation arises primarily from the significant nonlinearity of the thermodynamic relation $c^f_{\mathrm{SiO_2}}$–$\bar{\rho}\bar{c}_{\mathrm{SiO_2}}$ obtained from ThermoLab, whereas the explicit analytical solution assumes a piecewise-linear approximation of this relation. The analytical solution can be refined to account for the continuous nonlinear variation of the thermodynamic relation. This correction is derived in Appendix C and compared with the numerical results and the original analytical solution in Fig. C1.

https://doi.org/10.5194/egusphere-2026-4987
Preprint. Discussion started: 1 September 2026

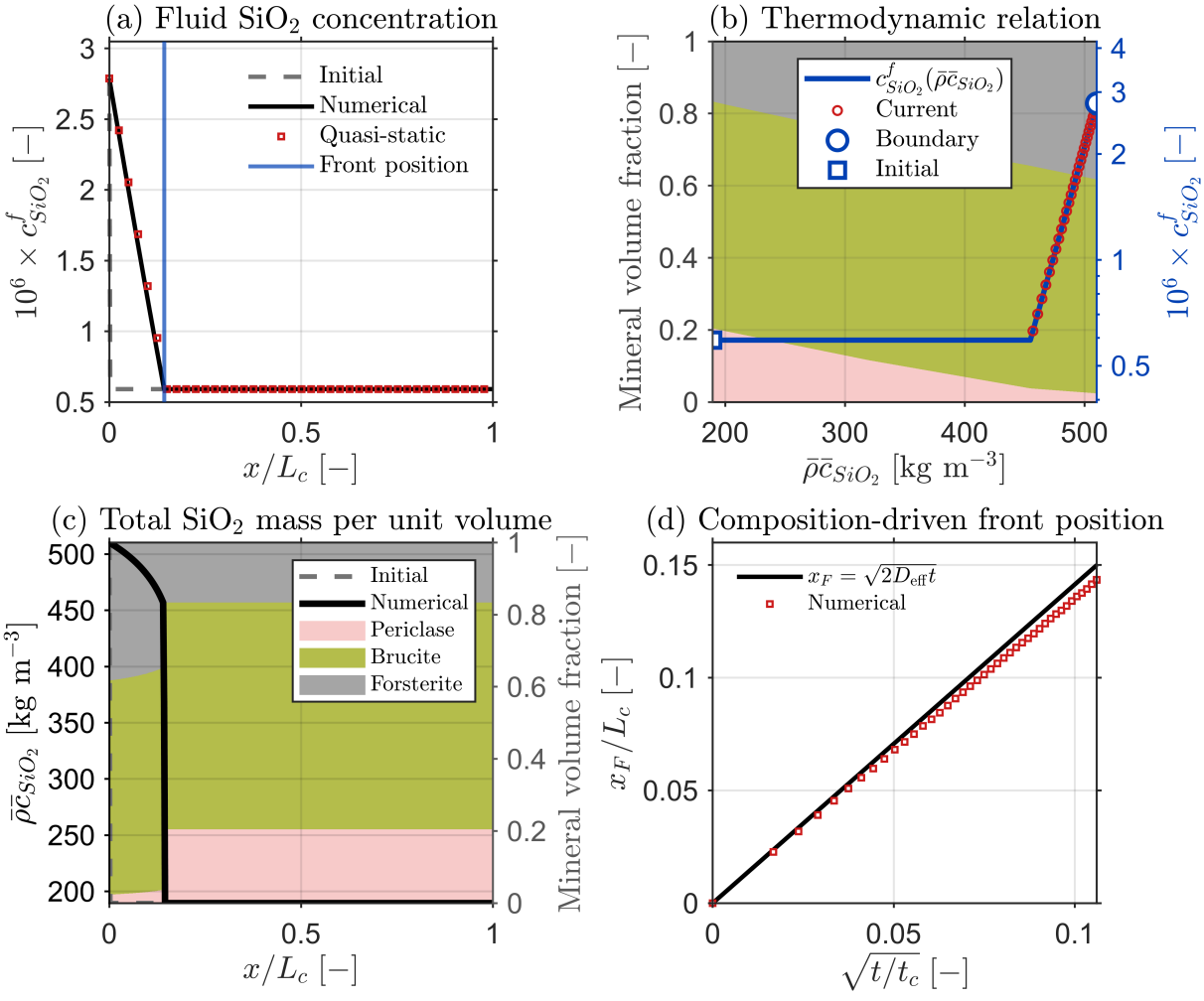

Figure 10. Numerical simulation of composition-driven reaction front and analytical solution. (a) Dissolved silica concentration profile, $c^f_{\mathrm{SiO_2}}(x,t)$, multiplied by 10^6 for display. The dashed grey curve shows the initial condition, the black curve the numerical solution, red symbols the quasi-steady analytical profile, and the blue line the numerical front position. (b) Thermodynamic $c^f_{\mathrm{SiO_2}}$–$\bar{\rho}\bar{c}_{\mathrm{SiO_2}}$ relation at $T = 500\,^\circ\mathrm{C}$ and $P^f = 10.0\,\mathrm{kbar}$. Colored regions show equilibrium mineral fractions, red symbols the numerical states, and the open circle and square the boundary and initial values, respectively, used in the numerical simulation. (c) Total silica mass per unit bulk volume, $\bar{\rho}\bar{c}_{\mathrm{SiO_2}}$, and mineral-volume-fraction profiles showing the propagating reaction front. The dashed grey curve shows the initial condition and the black curve the numerical solution. (d) Reaction-front position versus the square root of normalized time. The red symbols show the numerical solution and black line represents the analytical prediction, $x_F = \sqrt{2D_{\text{eff}}t}$, with $D_{\text{eff}} = D/L = 1.90 \times 10^{-9}\,\mathrm{m^2\,s^{-1}}$.

https://doi.org/10.5194/egusphere-2026-4987
Preprint. Discussion started: 1 September 2026

5 Discussion

5.1 Reaction–front diffusivity versus transport diffusivity

A fundamental consequence of the moving-boundary formulation is that the diffusivity governing reaction-front propagation generally differs from the physical diffusivity governing transport. The transported field evolves according to the thermal, hydraulic, or chemical diffusivity, whereas the reaction front propagates with an effective diffusivity that additionally accounts for the thermodynamic transformation across the moving interface.

The characteristic $\sqrt{t}$ scaling of reaction-front propagation, well known from the classical Stefan problem, is therefore not restricted to temperature-driven phase transitions. The same scaling arises for pressure- and composition-driven fronts when diffusive transport is coupled to a local equilibrium reaction at a moving boundary. Thus, $\sqrt{t}$ scaling indicates diffusive supply to the reaction front, but does not imply that the coefficient relating front position to time is the physical transport diffusivity.

The origin of this distinction follows directly from the conservative formulation, Eq. (14). The thermodynamic potential u, such as temperature, fluid pressure, or chemical potential, drives the diffusive flux, whereas A represents the corresponding conserved quantity per unit bulk volume, such as thermal energy, total mass, or total component mass (Fig. 7). In the diffusion-dominated limit, u remains continuous across the reaction front, although its gradient may be discontinuous. In contrast, A may exhibit a finite jump because the reaction changes the equilibrium state and associated properties, such as density, fluid or volatile content, and chemical storage. Conservation across this discontinuity gives the Rankine–Hugoniot jump condition, Eq. (6). The front velocity is therefore controlled jointly by the diffusive flux and the finite jump in conserved quantity across the reaction front.

This distinction has important implications for interpreting laboratory and field observations. A reaction front may follow the characteristic $\sqrt{t}$ scaling while propagating substantially more slowly than the underlying diffusive transport process. Slow front propagation therefore does not necessarily imply low thermal, hydraulic, or chemical diffusivity, or low permeability, but may instead reflect a large conserved-quantity jump associated with latent heat, density change, hydration or dehydration, volatile storage, or redistribution of a mobile component between fluid and solid phases. Consequently, a diffusivity inferred from $x_F \propto \sqrt{D_{\mathrm{eff}} t}$ should generally be interpreted as an effective front diffusivity that combines physical transport with the thermodynamic transformation across the reaction front.

5.2 Sharp reaction fronts: diffusive versus advective transport

Natural reaction fronts are often characterized by sharp changes in mineral assemblage or element concentrations (Austrheim, 1987; Ferry and Gerdes, 1998; Beinlich et al., 2020). Our model couples diffusive transport with equilibrium reactions and generates propagating sharp reaction fronts (Figs. 9 and 10). This behavior differs fundamentally from conventional advection–diffusion–reaction models (Ferry and Gerdes, 1998; Ague, 2014; Koehn et al., 2021; Penniston-Dorland, 2025), in which reactions are commonly represented by kinetic source terms without explicitly accounting for thermodynamic jumps across a moving reaction boundary. In such models, sharp reaction fronts typically require advection-dominated transport. In contrast, our moving-boundary formulation incorporates the finite jump in conserved quantity predicted by equilibrium thermodynamics

https://doi.org/10.5194/egusphere-2026-4987
Preprint. Discussion started: 1 September 2026

through the Rankine–Hugoniot condition, allowing sharp fronts to propagate under diffusion-dominated conditions. Their sharpness arises from the discontinuous transformation between local equilibrium states rather than from advection or an imposed kinetic mechanism. Thus, the occurrence of a sharp reaction front in natural rocks does not necessarily indicate advection-dominated transport; such fronts may also develop under diffusion-dominated conditions.

5.3 Scope and applicability of the analytical framework

The framework is intentionally formulated as a minimal model for the propagation of sharp reaction fronts. It retains only the essential ingredients required to couple equilibrium thermodynamics with diffusive transport while rigorously conserving energy or mass across the moving reaction boundary. Restricting the analysis to the diffusion-dominated limit reduces the governing equations to a simple ordinary differential equation for the reaction-front position, from which explicit closed-form solutions can be derived. These solutions provide a transparent asymptotic alternative to the implicit error-function solution of the classical Stefan problem and reveal the physical controls on reaction-front propagation.

An important advantage of the analytical formulation is that its validity can be assessed directly from equilibrium thermodynamics. The closed-form solutions are valid for sufficiently large values of the dimensionless L number ($L \gg 1$). The L number compares the finite jump in conserved quantity across the reaction front with the corresponding local conserved quantity change associated with the driving-field contrast. Both contributions are determined by the thermodynamic u–A relation and can be obtained from equilibrium thermodynamic calculations based on Gibbs energy minimization. The applicability of the analytical approximation can therefore be assessed independently of transport properties such as thermal diffusivity, permeability, or chemical diffusivity.

The L number also quantifies the influence of the thermodynamic transformation on front propagation. As L increases, the effective front diffusivity becomes progressively smaller than the physical transport diffusivity, resulting in stronger retardation of the reaction front. Consequently, the characteristic $\sqrt{t}$ scaling reflects diffusion-controlled supply coupled to an equilibrium transformation, rather than non-reactive diffusion alone.

The present framework provides a foundation for more general models. Future developments will incorporate advective transport, reaction kinetics, and the simultaneous evolution of multiple thermodynamic variables, such as temperature and chemical composition.

6 Conclusions

We developed a unified conservative moving-boundary framework for metamorphic reactions, fluid–rock interactions, and phase transitions. By coupling diffusive transport with local equilibrium thermodynamics through the Rankine–Hugoniot condition, the formulation shows that temperature-, pressure-, and composition-driven reaction fronts share the same mathematical structure despite their different physical driving mechanisms.

The theory yields explicit analytical expressions for reaction-front position and velocity and predicts the characteristic $\sqrt{t}$ scaling observed in experiments. In contrast to classical Stefan solutions, the present formulation avoids the error function and

https://doi.org/10.5194/egusphere-2026-4987
Preprint. Discussion started: 1 September 2026

numerical solution of a transcendental equation, providing a direct relation between front propagation, transport properties, and equilibrium thermodynamics.

A key result is that reaction-front propagation is governed by an effective diffusivity that generally differs from the physical thermal, hydraulic, or chemical transport diffusivity. This effective diffusivity combines transport with the finite thermodynamic transformation across the front and is quantified by the dimensionless L number. The L number can be evaluated from equilibrium thermodynamic calculations, thereby linking Gibbs energy minimization directly to reaction-front dynamics. Consequently, slow reaction-front propagation does not necessarily imply slow diffusive transport or low permeability, but may instead reflect a large thermodynamic change across the reaction.

The framework also demonstrates that sharp reaction fronts can propagate in the diffusion-dominated regime because finite jumps in material properties are explicitly represented across the moving interface. Sharp fronts therefore do not necessarily imply advection-dominated transport. More broadly, phase transitions, devolatilization, hydration, carbonation, leaching, and metasomatic fronts can be interpreted as manifestations of the same conservative moving-boundary dynamics. The resulting analytical solutions provide a simple basis for predicting and interpreting reaction-front propagation in natural and experimental systems.

Code and data availability. All numerical simulations, analytical evaluations, and figure-generation routines developed for this study were implemented in MATLAB using custom algorithms. Upon acceptance, the complete MATLAB source code, precomputed thermodynamic lookup tables, and documentation required to reproduce the results will be made openly available in a public repository. The equilibrium thermodynamic data used to construct Figures 2, 6, and 8, and to initialize the numerical simulations shown in Figures 9 and 10, were calculated using ThermoLab (Vrijmoed and Podladchikov, 2022). The experimental and observational data compiled in Figure 3 were digitized or reconstructed from the original studies cited in the figure caption. No new experimental data were generated in this study.

Appendix A: Quasi-steady advection–diffusion profile near a reaction front

We derive the quasi-steady advection–diffusion profile used in Sec. 2.2 and illustrated in Fig. 4a. The reaction front is located at $x = x_F(t)$, with reacted material occupying $0 \le x < x_F$ and unreacted material occupying $x > x_F$. For a prescribed instantaneous front position, transport in the reacted region satisfies

$$v_a \frac{du}{dx} - D\frac{d^2u}{dx^2} = 0, \qquad u(0) = u_{\mathrm{BC}}, \qquad u(x_F^-) = u_-. \tag{A1}$$

Here, v_a is the advection velocity, D is the transport diffusivity, u_{BC} is the imposed boundary value, and u_- is the reacted-side value at the front. Ahead of the front, the transported field is assumed to be spatially uniform, $u(x) = u_+$.

The one-sided front values are related by local thermodynamic equilibrium, and the driving-field contrast across the reacted region is

$$u_- = k_{\mathrm{eq}} u_+, \qquad \Delta u = u_{\mathrm{BC}} - u_-. \tag{A2}$$

https://doi.org/10.5194/egusphere-2026-4987
Preprint. Discussion started: 1 September 2026

For thermodynamic potentials such as temperature, fluid pressure, and chemical potential, $k_{\mathrm{eq}} = 1$ and u is continuous across the reaction front.

The general solution of Eq. (A1) in the reacted region is

$$u(x) = C_1 + C_2 \exp\left(\frac{v_a}{D} x\right). \tag{A3}$$

Introducing the Peclet number based on the instantaneous thickness of the reacted region,

$$Pe = \frac{v_a x_F}{D}, \tag{A4}$$

and applying the boundary conditions in Eq. (A1) gives the piecewise profile

$$u(x) = \begin{cases} u_- + \dfrac{\Delta u}{1 - \exp(-Pe)} \left[1 - \exp\left(\dfrac{v_a}{D}(x - x_F)\right)\right], & 0 \le x \le x_F, \\ u_+, & x > x_F. \end{cases} \tag{A5}$$

Equation (A5) describes the instantaneous transport profile for a prescribed x_F; the evolution of $x_F(t)$ must be determined independently from conservation across the moving interface.

In the diffusion-dominated limit, $Pe \ll 1$, expansion of the exponential terms in Eq. (A5) gives the approximately linear reacted-side profile

$$u(x) \simeq u_{\mathrm{BC}} - \Delta u \frac{x}{x_F}, \qquad 0 \le x \le x_F, \qquad Pe \ll 1. \tag{A6}$$

The corresponding gradient immediately behind the front is

$$\left.\frac{\partial u}{\partial x}\right|_{x_F^-} \simeq -\frac{\Delta u}{x_F}. \tag{A7}$$

This is the gradient used in the diffusion-dominated front-tracking derivation in Appendix B.

In the advection-dominated limit, $Pe \gg 1$, the transported field varies within a boundary layer of thickness $\delta = D/v_a$ immediately behind the front:

$$u(x) \simeq u_{\mathrm{BC}} - \Delta u \exp\left(\frac{x - x_F}{\delta}\right), \qquad \delta = \frac{D}{v_a}, \qquad 0 \le x \le x_F, \qquad Pe \gg 1. \tag{A8}$$

Thus, diffusion produces an approximately linear profile throughout the reacted region, whereas advection localizes the variation of u near the reaction front. In both limits, the equilibrium condition determines the one-sided front values, while conservation across the moving interface determines the front position and velocity.

Appendix B: Derivation of the quasi-steady front-tracking solution in the diffusion-dominated limit

This Appendix derives the reduced moving-front balance introduced in Sec. 2.3 and its closed-form solution given in Sec. 2.4. We start from the Rankine–Hugoniot condition, Eq. (6),

$$[A]\, v_F = -\left[K \frac{\partial u}{\partial x}\right] = \left(K \frac{\partial u}{\partial x}\right)_+ - \left(K \frac{\partial u}{\partial x}\right)_-, \qquad v_F = \frac{dx_F}{dt}. \tag{B1}$$

https://doi.org/10.5194/egusphere-2026-4987
Preprint. Discussion started: 1 September 2026

Here,

$$[A] = A_- - A_+, \tag{B2}$$

with A_- and A_+ denoting the one-sided values of the conserved quantity behind and ahead of the reaction front, respectively, as defined in Sec. 2.2.

In the diffusion-dominated limit, $Pe \ll 1$, the transported field behind the front is given by Eq. (A6),

$$u(x) \approx u_{\mathrm{BC}} - \Delta u \frac{x}{x_F}, \qquad 0 \le x \le x_F, \tag{B3}$$

where, following the main-text notation,

$$\Delta u = u_{\mathrm{BC}} - u_-. \tag{B4}$$

The gradient immediately behind the reaction front is therefore

$$\left.\frac{\partial u}{\partial x}\right|_{x_F^-} = -\frac{\Delta u}{x_F}. \tag{B5}$$

Ahead of the front, the field is assumed to be spatially uniform, so that

$$\left.\frac{\partial u}{\partial x}\right|_{x_F^+} \approx 0. \tag{B6}$$

Substitution of Eqs. (B5) and (B6) into Eq. (B1) gives

$$[A]\,\frac{dx_F}{dt} = K\frac{\Delta u}{x_F(t)}, \tag{B7}$$

which is the reduced moving-front condition given in Eq. (7).

Using $v_F = dx_F/dt$, Eq. (B7) gives

$$\frac{dx_F}{dt} = \frac{K\Delta u}{[A]}\frac{1}{x_F(t)}. \tag{B8}$$

Multiplying by $x_F(t)$,

$$x_F\,dx_F = \frac{K\Delta u}{[A]}\,dt. \tag{B9}$$

For $x_F(0) = 0$, integration from 0 to t gives

$$\int_0^{x_F(t)} \xi\,d\xi = \frac{K\Delta u}{[A]}\int_0^t d\tau, \tag{B10}$$

and therefore

$$\frac{x_F^2(t)}{2} = \frac{K\Delta u}{[A]}t. \tag{B11}$$

https://doi.org/10.5194/egusphere-2026-4987
Preprint. Discussion started: 1 September 2026

Using the effective front diffusivity defined in Eq. (9),

$$D_{\mathrm{eff}} = \frac{K\Delta u}{[A]}, \tag{B12}$$

the explicit front-position solution becomes

$$x_F(t) = \sqrt{2D_{\mathrm{eff}}t}, \tag{B13}$$

which is Eq. (8) of the main text. The corresponding front velocity is

$$v_F(t) = \frac{dx_F}{dt} = \frac{D_{\mathrm{eff}}}{x_F(t)} = \sqrt{\frac{D_{\mathrm{eff}}}{2t}}. \tag{B14}$$

Finally, using the local transport diffusivity

$$D = \frac{K}{A'_u}, \tag{B15}$$

defined in Eq. (13), Eq. (B12) can be written as

$$D_{\mathrm{eff}} = D\frac{A'_u\Delta u}{[A]}. \tag{B16}$$

With the dimensionless L number introduced in Eq. (11),

$$L = \frac{[A]}{A'_u\Delta u}, \tag{B17}$$

we recover

$$D_{\mathrm{eff}} = \frac{D}{L}, \tag{B18}$$

as given in Eq. (12). Thus, the closed-form solution separates the local diffusivity D controlling transport of the field u from the dimensionless L number controlling the retardation of the moving reaction front.

Appendix C: Correction to the quasi-steady front law for a piecewise-defined nonlinear thermodynamic u–A relation

The explicit reaction-front law applied in Sec. 4.2, $D_{\mathrm{eff}} = D/L$ and $x_F(t) = \sqrt{2D_{\mathrm{eff}}t}$, follows from the quasi-steady derivation in Appendix B. This leading-order approximation accounts for the finite change $[A] = A_- - A_+$ in the conserved quantity across the reaction front. Thermodynamic u–A relations are commonly piecewise defined, however, and the individual thermodynamic branches need not be linear. When an active reacted branch is nonlinear, representing it only through an effective slope does not capture the continuous variation of A as the transported field changes from u_- at the front to u_{BC} at the boundary. The incoming flux must then both advance the reaction front and change the conserved quantity within the already reacted material. An improved prediction must account for this within-branch nonlinearity, which motivates the correction derived below and

https://doi.org/10.5194/egusphere-2026-4987
Preprint. Discussion started: 1 September 2026

evaluated using the same thermodynamic and transport parameters as in Sec. 4.2. Its effect on the predicted front position is shown in Fig. C1. For constant K,

$$u(x,t) \simeq u_{\mathrm{BC}} - \Delta u \frac{x}{x_F(t)}, \qquad \Delta u = u_{\mathrm{BC}} - u_-, \qquad 0 \le x \le x_F. \tag{C1}$$

The total excess of the conserved quantity in the reacted layer relative to the initial unreacted state is

$$\mathcal{M}(t) = \int_0^{x_F(t)} [A(u) - A_+]\, dx. \tag{C2}$$

Substitution of Eq. (C1) gives

$$\mathcal{M}(t) = x_F \left([A] + \overline{\Delta A} \right), \qquad \overline{\Delta A} = \frac{1}{\Delta u} \int_{u_-}^{u_{\mathrm{BC}}} [A(u) - A_-]\, du. \tag{C3}$$

Here, $[A]$ is the finite change in the conserved quantity associated with transformation of fresh material across the reaction front, whereas $\overline{\Delta A}$ is the mean additional accumulation of the conserved quantity within material that has already reacted. Global conservation requires

$$\frac{d\mathcal{M}}{dt} = J_{\mathrm{BC}} = K \frac{\Delta u}{x_F}, \tag{C4}$$

where J_{BC} is the flux of the conserved quantity supplied through the left boundary. For fixed u_{BC} and u_-, Eqs. (C3) and (C4) yield

$$\left([A] + \overline{\Delta A} \right) \frac{dx_F}{dt} = K \frac{\Delta u}{x_F}, \qquad D_{\mathrm{eff}}^{(\mathrm{cor})} = \frac{K \Delta u}{[A] + \overline{\Delta A}}. \tag{C5}$$

Using the main-text definitions of A'_u, D, and L, and introducing the dimensionless correction factor Γ_{nl},

$$A'_u = \frac{A_{\mathrm{BC}} - A_-}{\Delta u}, \qquad D = \frac{K}{A'_u}, \qquad L = \frac{[A]}{A'_u \Delta u}, \qquad \Gamma_{\mathrm{nl}} = \frac{\overline{\Delta A}}{A'_u \Delta u}. \tag{C6}$$

Here, $A_{\mathrm{BC}} = A(u_{\mathrm{BC}})$ and A'_u is the secant thermodynamic response over the active reacted interval. The corrected front-propagation coefficient and front position are

$$D_{\mathrm{eff}}^{(\mathrm{cor})} = \frac{D}{L + \Gamma_{\mathrm{nl}}}, \qquad x_F(t) = \sqrt{2 D_{\mathrm{eff}}^{(\mathrm{cor})} t}. \tag{C7}$$

The closed-form analytical expression $D_{\mathrm{eff}} = D/L$ is recovered when the continuous variation of the conserved quantity behind the front is negligible, i.e., when $\Gamma_{\mathrm{nl}} \ll L$. In the piecewise-defined thermodynamic relation used in Sec. 4.2, only the active reacted interval $u_- \le u \le u_{\mathrm{BC}}$ enters the correction. Over this interval, the equilibrium relation calculated with ThermoLab (Vrijmoed and Podladchikov, 2022) is approximately linear in $\ln(u)$ and can be represented as

$$A(u) - A_- = (A_{\mathrm{BC}} - A_-) \frac{\ln(u/u_-)}{\ln r}, \qquad r = \frac{u_{\mathrm{BC}}}{u_-}, \qquad \Gamma_{\mathrm{nl}} = \frac{r \ln r - r + 1}{(r-1) \ln r}. \tag{C8}$$

https://doi.org/10.5194/egusphere-2026-4987
Preprint. Discussion started: 1 September 2026

With $r = 4.717$, $L = 4.781$, and $D \simeq 9.09 \times 10^{-9}\,\mathrm{m^2\,s^{-1}}$, this gives

$$\Gamma_{\mathrm{nl}} = 0.624, \qquad D_{\mathrm{eff}} = \frac{D}{L} \simeq 1.90 \times 10^{-9}\,\mathrm{m^2\,s^{-1}}, \qquad D_{\mathrm{eff}}^{(\mathrm{cor})} \simeq 1.68 \times 10^{-9}\,\mathrm{m^2\,s^{-1}}. \tag{C9}$$

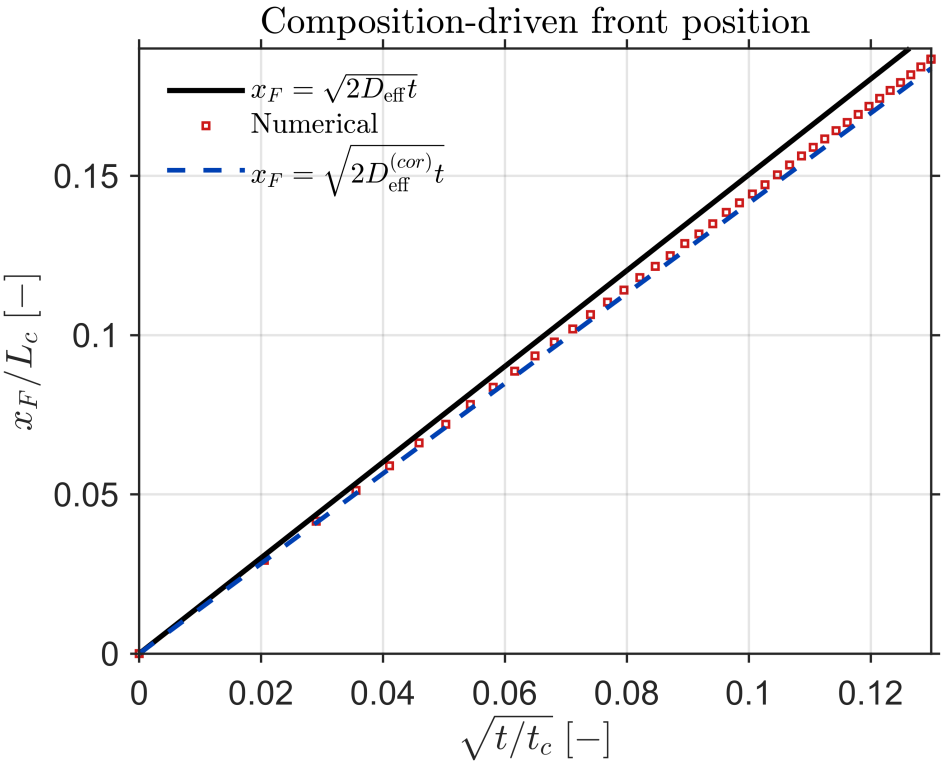

Figure C1. Reaction-front position as a function of the square root of normalized time for the composition-driven example in Sec. 4.2. The red symbols show the front position obtained from the numerical calculation. The black line shows the leading-order closed-form prediction, $x_F = \sqrt{2D_{\mathrm{eff}}t}$, with $D_{\mathrm{eff}} = D/L = 1.90 \times 10^{-9}\,\mathrm{m^2\,s^{-1}}$. The dashed blue line shows the analytical prediction corrected to account for the nonlinear variation of the thermodynamic relation $A(u)$, $x_F = \sqrt{2D_{\mathrm{eff}}^{(\mathrm{cor})}t}$, with $D_{\mathrm{eff}}^{(\mathrm{cor})} = D/(L + \Gamma_{\mathrm{nl}}) = 1.68 \times 10^{-9}\,\mathrm{m^2\,s^{-1}}$ and $\Gamma_{\mathrm{nl}} = 0.624$. Neither analytical prediction contains parameters fitted to the numerical front position.

As shown in Fig. C1, the leading-order solution slightly overpredicts the propagation rate of the numerical front. Accounting for the continuous accumulation of the conserved quantity along the piecewise-defined nonlinear thermodynamic u–A relation reduces the effective front-propagation coefficient and brings the closed-form prediction into closer agreement with the numerical result. All quantities entering the correction are determined independently from the transport parameters and the equilibrium thermodynamic relation; none is fitted to the numerical front position.

Author contributions. L.K. conceived and led the study, formulated the unified theoretical and moving-boundary framework, derived the analytical solutions, designed and implemented the numerical models and research codes, performed the simulations, validation, and bench-

https://doi.org/10.5194/egusphere-2026-4987
Preprint. Discussion started: 1 September 2026

marking, analyzed and interpreted the results, produced the numerical visualizations, and wrote the original manuscript. S.M.S. contributed to the design and refinement of the conceptual framework, interpretation of the results, and critical scientific refinement and editing of the manuscript. Y.P. contributed to the conceptual development and methodology of the study, interpretation of the results, and review and editing of the manuscript.

580 *Acknowledgements.*

https://doi.org/10.5194/egusphere-2026-4987
Preprint. Discussion started: 1 September 2026

References

Ague, J. J.: 4.6—Fluid Flow in the Deep Crust, in: Treatise on Geochemistry, edited by Holland, H. D. and Turekian, K. K., pp. 203–247, Elsevier, 2nd edn., https://doi.org/10.1016/B978-0-08-095975-7.00306-5, 2014.

Amiri, H., Dialeismas, V., Freitas, D., Rizzo, R., Chogani, A., Schlepütz, C. M., Fusseis, F., and Plümper, O.: Transient Porosity During Fluid-Mineral Interaction. Part 1: In Situ 4D Tomography, Journal of Geophysical Research: Solid Earth, 131, e2025JB032 881, https://doi.org/https://doi.org/10.1029/2025JB032881, e2025JB032881 2025JB032881, 2026.

Austrheim, H.: Eclogitization of lower crustal granulites by fluid migration through shear zones, Earth and Planetary Science Letters, 81, 221–232, https://doi.org/https://doi.org/10.1016/0012-821X(87)90158-0, 1987.

Beinlich, A., John, T., Vrijmoed, J. C., et al.: Instantaneous rock transformations in the deep crust driven by reactive fluid flow, Nature Geoscience, 13, 307–311, https://doi.org/10.1038/s41561-020-0554-9, 2020.

Bras, E., Yamato, P., Schmalholz, S. M., Duretz, T., and Podladchikov, Y. Y.: Eclogitisation of dry and impermeable granulite by fluid flow with reaction-induced porosity: Insights from hydro-chemical modelling, Earth and Planetary Science Letters, 617, 118 256, https://doi.org/https://doi.org/10.1016/j.epsl.2023.118256, 2023.

Coussy, O.: Poromechanics, John Wiley Sons, Chichester, England, ISBN 978-0-470-84920-0, https://onlinelibrary.wiley.com/doi/book/10.1002/0470092718, 2004.

Ding, X., Harlov, D. E., Chen, B., and Sun, W.: Fluids, Metals, and Mineral/Ore Deposits, Geofluids, 2018, 1452 409, https://doi.org/10.1155/2018/1452409, 2018.

Ferry, J. M. and Gerdes, M. L.: Chemically Reactive Fluid Flow During Metamorphism, Annual Review of Earth and Planetary Sciences, 26, 255–287, https://doi.org/10.1146/annurev.earth.26.1.255, 1998.

Fusseis, F., Schrank, C., Liu, J., Karrech, A., Llana-Fúnez, S., Xiao, X., and Regenauer-Lieb, K.: Pore formation during dehydration of a polycrystalline gypsum sample observed and quantified in a time-series synchrotron X-ray micro-tomography experiment, Solid Earth, 3, 71–86, https://doi.org/10.5194/se-3-71-2012, 2012.

Gupta, S. C.: The classical Stefan problem: basic concepts, modelling and analysis with quasi-analytical solutions and methods, vol. 45, Elsevier, 2017.

Hacker, B. R.: Subduction Factory 1. Theoretical Mineralogy, Densities, Seismic Wave Speeds, and H_2O Contents, Journal of Geophysical Research: Solid Earth, 108, 2029, https://doi.org/10.1029/2001JB001127, 2003.

Holland, T. and Powell, R.: An internally consistent thermodynamic data set for phases of petrological interest, Journal of metamorphic Geology, 16, 309–343, 1998.

Huet, B., Tasoti, V., and Khalfallah, I.: A review of Portland cement carbonation mechanisms in CO2 rich environment, Energy Procedia, 4, 5275–5282, 2011.

John, T., Gussone, N., Podladchikov, Y., et al.: Volcanic arcs fed by rapid pulsed fluid flow through subducting slabs, Nature Geoscience, 5, 489–492, https://doi.org/10.1038/ngeo1482, 2012.

Khakimova, L., Schmalholz, S. M., and Podladchikov, Y. Y.: Beyond hydraulic diffusion: reaction front propagation and timescales in metamorphic (de)volatilization processes, EGUsphere, pp. 1–34, https://doi.org/10.5194/egusphere-2026-3107, preprint, discussion started 15 June 2026, 2026.

https://doi.org/10.5194/egusphere-2026-4987
Preprint. Discussion started: 1 September 2026

Koehn, D., Piazolo, S., Beaudoin, N. E., Kelka, U., Spruženiece, L., Putnis, C. V., and Toussaint, R.: Relative rates of fluid advection, elemental diffusion and replacement govern reaction front patterns, Earth and Planetary Science Letters, 565, 116 950, https://doi.org/https://doi.org/10.1016/j.epsl.2021.116950, 2021.

LeVeque, R. J.: Finite Volume Methods for Hyperbolic Problems, Cambridge Texts in Applied Mathematics, Cambridge University Press, Cambridge, UK, ISBN 9780521009249, https://doi.org/10.1017/CBO9780511791253, 2002.

Lichtner, P. C.: Continuum Formulation of Multicomponent-Multiphase Reactive Transport, in: Reactive Transport in Porous Media, edited by Lichtner, P. C., Steefel, C. I., and Oelkers, E. H., vol. 34 of *Reviews in Mineralogy*, pp. 1–82, Mineralogical Society of America, Washington, DC, https://doi.org/10.1515/9781501509797-004, 1996.

Lichtner, P. C., Oelkers, E. H., and Helgeson, H. C.: Interdiffusion with multiple precipitation/dissolution reactions: Transient model and the steady-state limit, Geochimica et Cosmochimica Acta, 50, 1951–1966, https://doi.org/https://doi.org/10.1016/0016-7037(86)90251-6, 1986.

Mainguy, M. and Coussy, O.: Propagation Fronts during Calcium Leaching and Chloride Penetration, Journal of Engineering Mechanics, 126, 250–257, https://doi.org/10.1061/(ASCE)0733-9399(2000)126:3(250), 2000.

Malvoisin, B., Podladchikov, Y. Y., and Vrijmoed, J. C.: Coupling changes in densities and porosity to fluid pressure variations in reactive porous fluid flow: Local thermodynamic equilibrium, Geochemistry, Geophysics, Geosystems, 16, 4362–4387, https://doi.org/https://doi.org/10.1002/2015GC006019, 2015.

Matter, J. M. and Kelemen, P. B.: Permanent storage of carbon dioxide in geological reservoirs by mineral carbonation, Nature Geoscience, 2, 837–841, https://doi.org/10.1038/ngeo683, 2009.

Mazzucchelli, M. L., Moulas, E., Kaus, B. J., and Speck, T.: Fluid-mineral Equilibrium Under Nonhydrostatic Stress: Insight From Molecular Dynamics, American Journal of Science, 324, 2, https://doi.org/10.2475/001c.92881, 2024.

Mazzucchelli, M. L., Moulas, E., Schmalholz, S. M., Kaus, B. J. P., and Speck, T.: Instability of Fluid-Mineral Equilibrium Under Non-Hydrostatic Stress Investigated With Molecular Dynamics, Journal of Geophysical Research: Solid Earth, 131, e2025JB033 520, https://doi.org/https://doi.org/10.1029/2025JB033520, e2025JB033520 2025JB033520, 2026.

McKenzie, D.: The Generation and Compaction of Partially Molten Rock, Journal of Petrology, 25, 713–765, https://doi.org/10.1093/petrology/25.3.713, 1984.

Nauman, E. B. and He, D. Q.: Nonlinear diffusion and phase separation, Chemical Engineering Science, 56, 1999–2018, https://doi.org/10.1016/S0009-2509(01)00005-7, 2001.

Padrón-Navarta, J. A., Hermann, J., Garrido, C. J., López Sánchez-Vizcaíno, V., and Gómez-Pugnaire, M. T.: Metamorphic record of high-pressure dehydration of antigorite serpentinite to chlorite harzburgite in a subduction setting (Cerro del Almirez, Nevado–Filábride Complex, Southern Spain), Journal of Petrology, 52, 2047–2078, https://doi.org/10.1093/petrology/egr039, 2011.

Penniston-Dorland, S. C.: Fluids in metamorphic systems, in: Treatise on Geochemistry (Third edition), edited by Anbar, A. and Weis, D., pp. 495–531, Elsevier, Oxford, third edition edn., ISBN 978-0-323-99763-8, https://doi.org/https://doi.org/10.1016/B978-0-323-99762-1.00040-1, 2025.

Philpotts, A. R. and Ague, J. J.: Principles of Igneous and Metamorphic Petrology, Cambridge University Press, 3 edn., 2022.

Porkoláb, K., Moulas, E., and Schmalholz, S. M.: Modeling the interplay between reaction progress, deformation and stress field evolution during antigorite dehydration: Implications for intermediate-depth seismicity, Geophysical Research Letters, 52, e2024GL113 865, https://doi.org/10.1029/2024GL113865, 2025.

https://doi.org/10.5194/egusphere-2026-4987
Preprint. Discussion started: 1 September 2026

Schmalholz, S. M., Moulas, E., Plümper, O., Myasnikov, A. V., and Podladchikov, Y. Y.: 2D hydro-mechanical-chemical modeling of (de)hydration reactions in deforming heterogeneous rock: The periclase-brucite model reaction, Geochemistry, Geophysics, Geosystems, 21, e2020GC009 351, 2020.

Schmalholz, S. M., Khakimova, L., Podladchikov, Y., Bras, E., Yamato, P., and John, T.: (De)hydration Front Propagation Into Zero-Permeability Rock, Geochemistry, Geophysics, Geosystems, 25, e2023GC011 422, https://doi.org/https://doi.org/10.1029/2023GC011422, e2023GC011422 2023GC011422, 2024.

Schmidt, M. W. and Poli, S.: Experimentally based water budgets for dehydrating slabs and consequences for arc magma generation, Earth and Planetary Science Letters, 163, 361–379, https://doi.org/10.1016/S0012-821X(98)00142-3, 1998.

Stefan, J.: Über die Theorie der Eisbildung, insbesondere über die Eisbildung im Polarmeere, Annalen der Physik, 278, 269–286, 1891.

Taetz, S., John, T., Bröcker, M., Spandler, C., and Stracke, A.: Fast intraslab fluid-flow events linked to pulses of high pore fluid pressure at the subducted plate interface, Earth and Planetary Science Letters, 482, 33–43, https://doi.org/10.1016/j.epsl.2017.10.044, 2018.

Thiévenaz, V., Séon, T., and Josserand, C.: Solidification dynamics of an impacted drop, Journal of Fluid Mechanics, 874, 756–773, 2019.

Turcotte, D. L. and Schubert, G.: Geodynamics, Cambridge University Press, Cambridge, UK, 3rd edn., ISBN 978-1107006539, https://doi.org/10.1017/CBO9780511843877, 2014.

Vrijmoed, J. C. and Podladchikov, Y. Y.: Thermolab: A thermodynamics laboratory for nonlinear transport processes in open systems, Geochemistry, Geophysics, Geosystems, 23, e2021GC010 303, 2022.